doi:10.26443/seismica.v4i2.1772

The Deep Lithospheric Structure of the South Australian Craton Revealed by Teleseismic Rayleigh Wave Tomography

John Paul O'Donnell [*] [†] [1], **Kate Selway** [2], **Claire E. Wade** [1], **Stephan Thiel** [3], **Caroline M. Eakin** [4], **Robert Pickle** [4], **Shubham Agrawal** [‡] [4], **Bruce Goleby** [5], **Alexei Gorbatov** [6]

[1]Geological Survey of South Australia, SA, Australia, [2]Vox Geophysics, WA, Australia, [3]CSIRO, SA, Australia, [4]Research School of Earth Sciences, Australian National University, ACT, Australia, [5]OPM Consulting, Canberra, ACT, Australia, [6]Geoscience Australia, ACT, Australia

Author contributions: *Formal Analysis*: John Paul O'Donnell. *Writing - Original draft*: John Paul O'Donnell, Kate Selway, Claire E. Wade. *Writing - Review & Editing*: John Paul O'Donnell, Kate Selway, Claire E. Wade, Stephan Thiel, Caroline M. Eakin, Robert Pickle, Shubham Agrawal, Bruce Goleby, Alexei Gorbatov.

Abstract We used teleseismic Rayleigh waves recorded by three recent broadband seismic arrays in southern Australia to develop a shear wave velocity model of the South Australian Craton from the lower crust to 250 km depth and compare this with isotope data, xenolith data, and 3D mantle resistivity structure. At ∼75–150 km depth, the seismic expression of cratonic core lithosphere encompasses the eastern Gawler Craton, Curnamona Province, and intervening Adelaide Superbasin north of ∼33° S. The inference of contiguous cratonic lithospheric mantle between the Gawler Craton and Curnamona Province may have implications for models of Rodinia breakup. Cratonic core lithospheric mantle is modelled as terminating substantially inboard of the conventionally-defined western margin of the Gawler Craton, but extending southward and northeastward beyond the conventionally-defined Curnamona Province boundary. Geophysical signatures of cratonic core lithospheric mantle are absent under the southern Eyre Peninsula, possibly related to the Jurassic–Cretaceous separation of Australia and Antarctica. At depths >150 km, the deep cratonic keel is restricted to the eastern Gawler Craton and southern Curnamona Province. Major iron oxide-copper-gold (IOCG) deposits of the eastern Gawler Craton (e.g., Olympic Dam) and Curnamona Province reside above the seismically fastest lithospheric mantle in the region. This seismic signature might provide a useful precompetitive vector for IOCG prospectivity mapping.

Production Editor: Yen Joe Tan
Handling Editor: Chiara Civiero
Copy & Layout Editor: Tara Nye

Received: June 4, 2025
Accepted: December 16, 2025
Published: December 23, 2025

1 Introduction

The South Australian lithosphere serves as an archive for over three billion years of Earth's evolution (e.g., Myers et al., 1996; Huston et al., 2012). This history includes the formation of an Archean cratonic core, lithospheric-scale Proterozoic reworking, a major mineralising event that produced world-class iron oxide-copper-gold (IOCG) deposits, Neoproterozoic rifting that produced basins in excess of 10 km thick, and most recently the Mesozoic rifting of Australia from Antarctica (e.g., Hand et al., 2007; Reid and Hand, 2012).

Seismic velocity is sensitive to temperature and bulk composition, thus velocity variations can be used to map lithospheric architecture (e.g., older, depleted versus younger, fertile domains in the lithospheric mantle). Continental-scale seismic tomography models of the Australian lithosphere have thus illuminated the contrast between the thick, seismically fast lithosphere of Precambrian western Australia and the thinner, seismically slower lithosphere of Phanerozoic eastern Australia (e.g., Fichtner et al., 2010; Fishwick and Rawlinson, 2012; Kennett et al., 2012; Yoshizawa, 2014; Yoshizawa and Kennett, 2015; Sun and Kennett, 2016; Wei et al., 2018; de Laat et al., 2023; Magrini et al., 2023). However, the hitherto sparse and uneven distribution of broadband seismic stations across southern Australia means that lithospheric mantle structure is reliably constrained only at a length scale of ∼3° and greater (e.g., Kennett et al., 2012). Higher resolution regional tomography models are key to progressing understanding of the detailed internal configuration of both Precambrian and Phanerozoic Australia, and hence continental evolution and corollaries such as mineral potential.

In this study, we used teleseismic surface waves recorded on three recently deployed temporary dense broadband seismic arrays to develop Rayleigh wave phase velocity maps of southern Australia at periods 20–167 s, and in turn, a vertically-polarised shear wave velocity (V_{SV}) model of the South Australian Craton from the lower crust to 250 km depth. Using the proxy of anomalously elevated V_{SV} values in the lithospheric mantle, we map the deep core of the South Australian Craton and compare our model with isotope data, xenolith data, and 3D mantle resistivity structure from magnetotelluric (MT) data.

*Corresponding author: john.odonnell@dmpe.wa.gov.au
†Now at Geological Survey of Western Australia, WA, Australia
‡Now at School of the Earth, Ocean and Environment, University of South Carolina, USA

2 Tectonic Framework

The North, West, and South Australian cratons are the nuclei of Precambrian Australia. In turn, the Gawler Craton and Curnamona Province are the nuclei of the South Australian Craton (e.g., Myers et al., 1996). The Gawler Craton is largely comprised of Paleo-to-Mesoproterozoic rocks encasing a late Archean core (e.g., Hand et al., 2007; Reid and Hand, 2012). The southern edge of the Gawler Craton is defined by the continental margin developed during the Jurassic–Cretaceous separation of Australia and Antarctica, but the craton's western margin (which abuts the mid-Neoproterozoic–Early Paleozoic Officer Basin), northern margin (which abuts the Meso-Neoproterozoic Musgrave Province), and eastern margin (which abuts the Neoproterozoic-Middle-Cambrian Adelaide Superbasin) are obscured by sedimentary cover and are less defined (e.g., Preiss et al., 1993; Preiss, 2000; Wade et al., 2008; Reid and Hand, 2012; Lloyd et al., 2020b; Agrawal et al., 2022). The Paleo–Mesoproterozoic Curnamona Province, which protrudes into the Phanerozoic terranes of eastern Australia, is distinguished by its near-circular expression in aeromagnetic data (e.g., Williams et al., 2009). Intermittent exposures of the crystalline basement underlying the Adelaide Superbasin show geological affinities to parts of the Gawler Craton and Curnamona Province, supporting their former juxtaposition (e.g., Szpunar et al., 2007; Morrissey et al., 2013).

2.1 Mineralisation

The major mineralising interval in the Gawler Craton occurred at ca. 1595–1575 Ma and involved the formation of the IOCG deposits of the Olympic Cu–Au Province, including the namesake Olympic Dam deposit, as well as related IOCG deposits in the Curnamona Province (e.g., Skirrow et al., 2007; Hand et al., 2007; Reid, 2019), and some gold-dominated mesothermal deposits of the Central Gawler Gold Province (e.g., Budd and Skirrow, 2007; Skirrow et al., 2007; Hand et al., 2007; Reid, 2019). IOCG mineralisation was contemporaneous with the widespread bimodal volcanic and intrusive activity associated with the Gawler Range Volcanics and Hiltaba Suite. Geological and temporal similarities between the Gawler Range Volcanics and Hiltaba Suite in the Gawler Craton, and the Benagerie Volcanic Suite and Ninnerie Supersuite granites in the Curnamona Province, respectively, suggest that the igneous suites comprise a formerly contiguous large igneous province, linking Cu–Au mineralisation in the Curnamona Province with the Olympic Cu–Au Province (e.g., Wade, 2011; Wade et al., 2012; Armistead et al., 2018; Jagodzinski et al., 2023).

3 Lithospheric Architecture and IOCG Formation

IOCG deposits were recognised as a new deposit type in the mid 1980s to early 1990s, but the extreme diversity of deposits has hindered formalisation of an agreed set of defining characteristics (e.g., Groves et al., 2010; Skirrow, 2022; Groves and Santosh, 2023). In terms of lithospheric architecture, Groves et al. (2010) note that world-class to giant Precambrian IOCG deposits are located close to the margins of Archean or Palaeoproterozoic cratons and suggest that partial melting of previously metasomatised subcontinental lithospheric mantle provides a magmatic-hydrothermal fluid source. Others have similarly commented on the role of a primed, metasomatised subcontinental lithospheric mantle, but differed in inferences of geodynamic context. For instance, Hitzman et al. (1992) reference spatial and temporal association with extensional tectonics for Precambrian IOCG formation, and Groves et al. (2010) suggest that mantle plumes might play a role. In the case of the Gawler Craton, Betts et al. (2009) suggest that migration of the craton and adjacent subduction zone over a mantle plume ultimately facilitated Mesoproterozoic IOCG formation, while Skirrow et al. (2018) suggest foundering of thickened, previously metasomatised lithospheric mantle to be the driver. Skirrow (2022) recently proposed an enhanced classification of IOCG deposits, but in terms of setting, again cites the role of previously metasomatised lithospheric mantle and emphasises that major IOCG provinces globally are preferentially located at or near craton margins. Constraining the lithospheric structure of the South Australian Craton provides essential context for interpreting the tectonic and metallogenic evolution of the Gawler Craton and Curnamona Province.

4 Seismic Arrays

The transportable SKIPPY broadband seismic array, which moved across Australia in the mid 1990s with a station spacing of ∼400 km, represented the first deliberate, systematic effort to unveil the 3D lithospheric seismic architecture of an entire continent (van der Hilst et al., 1994; Zielhuis and Hilst, 1996). Since then, various temporary seismic arrays have offered progressive enhancements in resolution. With regard to southern Australia, these have included linear broadband transects (e.g., BILBY, MARLA; Sippl, 2016; Liang and Kennett, 2020), sparse broadband arrays (e.g., SOC, TASMAL, ASR) and the patchwork of dense, regular arrays of short-period instruments comprising the WOMBAT experiment (e.g., Rawlinson et al., 2014). The temporary arrays have been supplemented by backbone permanent stations of the Australian National Seismic Network and Australian Seismometers in Schools program.

Seismic coverage across South Australia has been enhanced in recent years by the Lake Eyre Basin, AusArray SA, and SNAKEY seismic arrays (Figure 1). The 2018–2022 Lake Eyre Basin array (Eakin, 2019) consisted of 22 Nanometrics Trillium Compact 120 s broadband sensors and 18 Lennartz Electronic LE-3Dlite 1 Hz short-period sensors arranged in a triangular configuration around Kati Thanda–Lake Eyre. The 2020–2022 AusArray SA seismic array (O'Donnell et al., 2020) consisted of 28 Trillium Compact 120 s sensors and 10 Trillium Compact 20 s sensors arranged in a regular grid with ∼0.5° spacing across the eastern-central Gawler Craton. The 2023–2025 Seismic Network Around Kangaroo Eyre

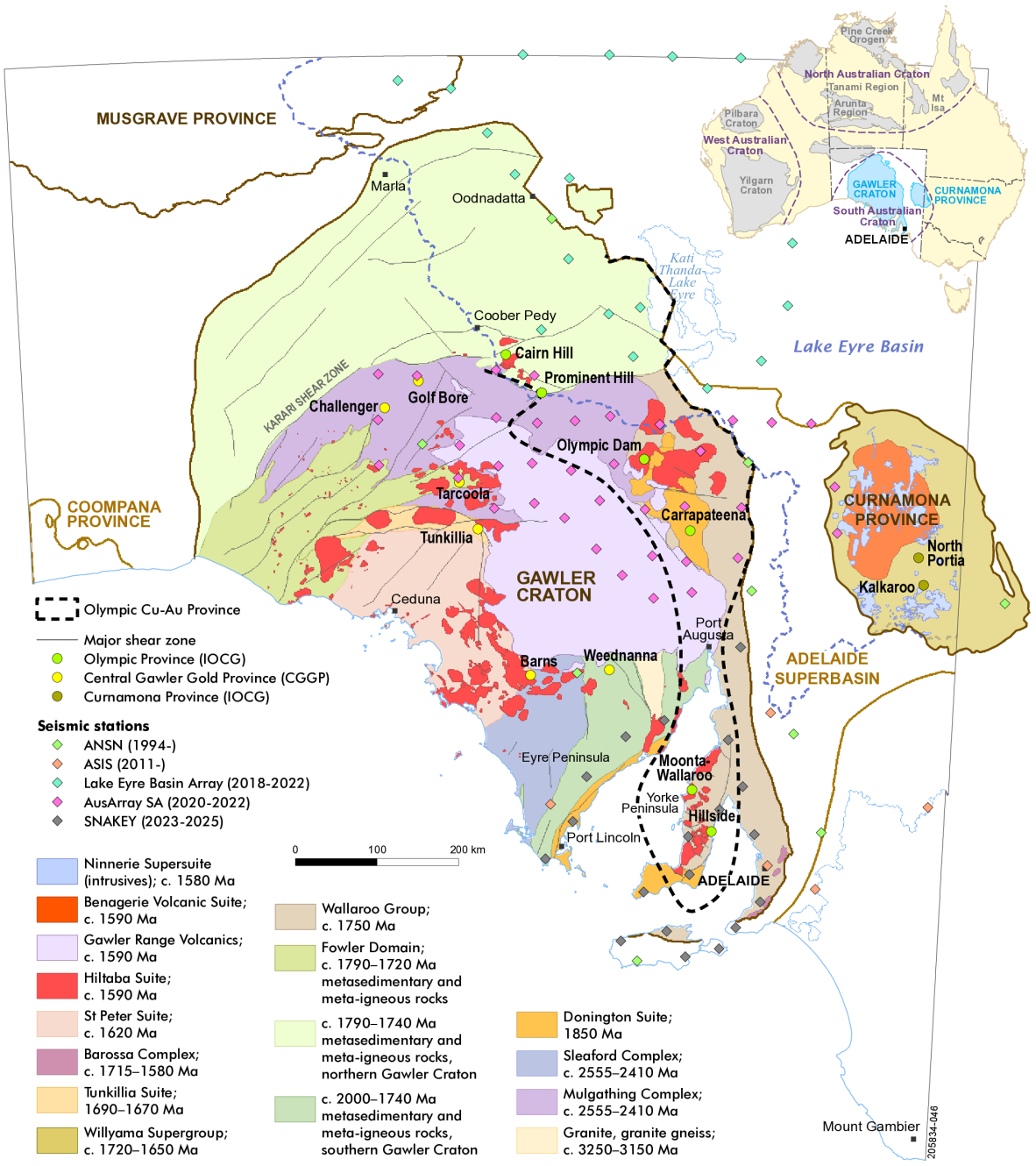

Figure 1 Simplified solid geology map of the Gawler Craton and Curnamona Province, the nuclei of the South Australian Craton. Lime green dots show the locations of significant iron oxide-copper-gold (IOCG) deposits of the Olympic Cu–Au Province (OP); olive green dots show the locations of significant IOCG deposits of the Curnamona Province (CP); yellow dots show the locations of significant gold deposits of the Central Gawler Gold Province (CGGP). Diamond symbols show the locations of the permanent and temporary broadband seismic stations used in this study.

Yorke (SNAKEY; Caroline M. Eakin and Robert Pickle, 2023) uses 12 Trillium Compact 120 s and eight Trillium Compact Posthole 120 s sensors. These three arrays all record three-component data at 100 samples per second.

5 Two-Plane-Wave Tomography

Accounting for off-great-circle path propagation and multipathing of surface waves is necessary in developing high-fidelity seismological Earth models (e.g., Evernden, 1953; Capon, 1970; Lay and Kanamori, 1985; Woodhouse and Wong, 1986; Friederich et al., 1994; Laske, 1995; Spetzler et al., 2001; Forsyth and Li, 2005). Motivated by observations reminiscent of wave interference across regional seismic arrays, Forsyth et al. (1998) cast the wavefield as the superposition of two interfering plane waves. With the caveat that the validity of the plane wave assumption depends on the array aperture, this modelling approach demonstrably improved

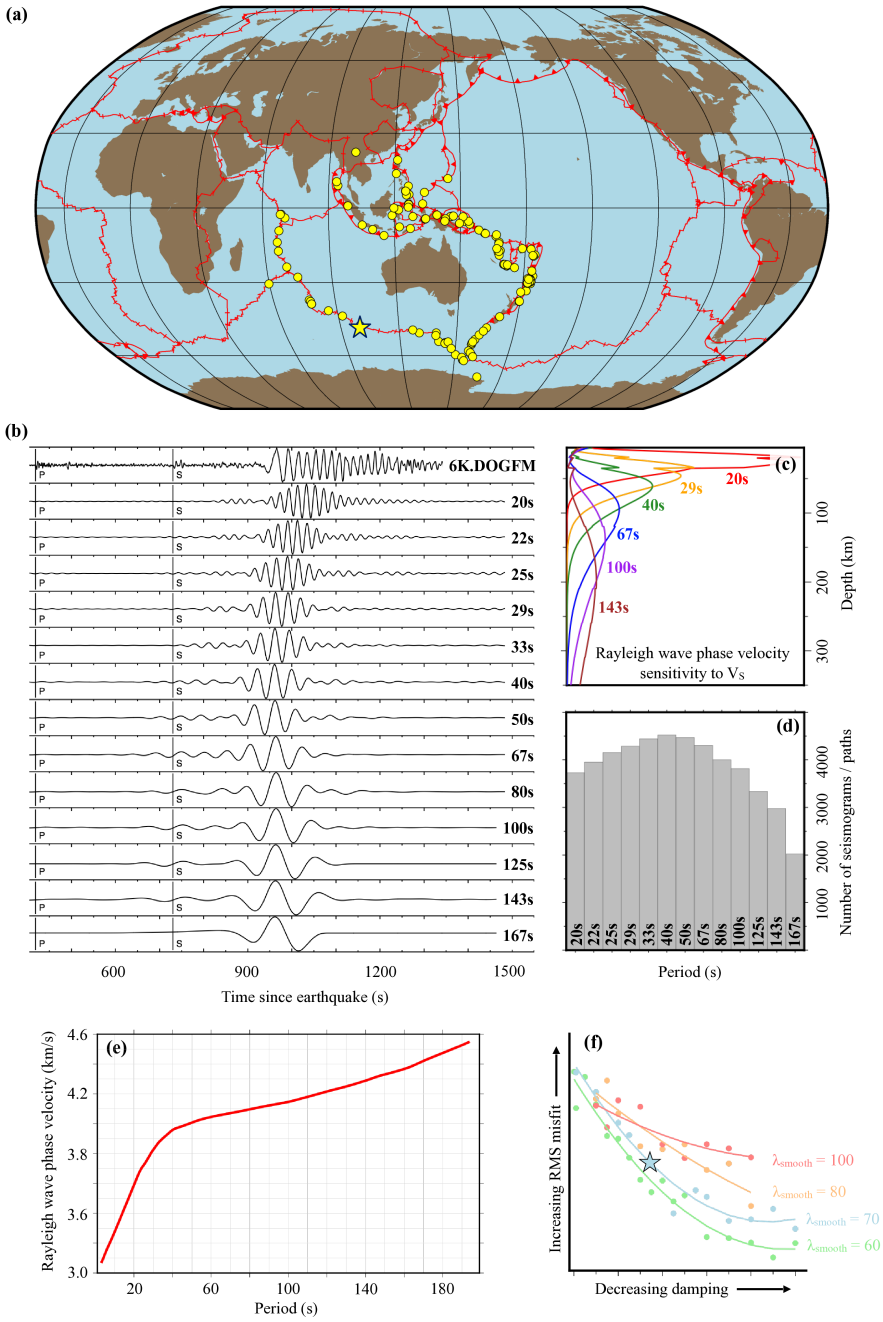

Figure 2 (a) Geographic distribution of the 142 earthquakes used in this study; (b) raw vertical-component seismogram from AusArray SA seismic station DOGFM (top) capturing a February 4th 2022 magnitude 6.3 Southeast Indian Ridge earthquake (star in (a)). Predicted arrival times of compressional (P) and shear (S) body waves according to the AK135 Earth model (Kennett et al., 1995) are marked, after which follows the larger amplitude Rayleigh wave. The dispersive nature of Rayleigh waves – the dependence of wave velocity on frequency – is made explicit by filtering the raw seismogram into 13 × 10 mHz wide frequency bands with centre periods ranging from 20 to 167 s; (c) sensitivity kernels of fundamental mode Rayleigh wave phase velocities to shear wave velocity structure at periods 20, 29, 40, 67, 100 and 143 s calculated for the AK135 Earth model; the sensitivity kernels peak deeper, are broader and heavier tailed as the period increases; (d) Number of seismograms yielding viable Rayleigh wave phase velocity measurements as a function of period to constrain the tomography; (e) Reference Rayleigh wave phase velocity dispersion curve for southern Australia derived by merging 1D average curves for southern Australia (3-20 s; O'Donnell et al., 2023) and continental Australia (4-200 s; Magrini et al., 2023); (f) trade-off curves illustrating the selection of optimal smoothing and damping regularisation for the 25 s period Rayleigh wave phase velocity tomography. Each curve represents the trade-off between model damping – the permitted deviation from a starting model – and data fitting for a given model smoothing length scale. We concluded that a damping value of 0.4 and smoothing length scale of 70 km (blue star) represented a good compromise between data fitting and model complexity. All phase velocity models subsequently displayed were determined using this regularisation.

data fitting relative to single plane wave representations (e.g., Li et al., 2003). So-called two-plane-wave tomography has since usefully illuminated lithospheric structure across diverse tectonic settings (e.g., Weeraratne et al., 2003; Yang and Forsyth, 2006b; Harmon et al., 2009; O'Donnell et al., 2019).

We applied the two-plane-wave method to fundamental mode Rayleigh waves recorded on the Lake Eyre Basin, AusArray SA, SNAKEY, Australian National Seismic Network, and Australian Seismometers in Schools arrays over the period August 2019 to September 2023. To garner good quality waveforms for analysis, we screened earthquakes with magnitudes ≥ 6.0 occurring within the epicentral distance range $25^\circ < \Delta < 60^\circ$ of the composite seismic array. If multiple earthquakes clustered in space and time (i.e., a mainshock and aftershocks), we screened only the mainshock. Following instrument response deconvolution, a visual perusal of vertical-component record sections in four filter bands (full bandwidth; 25–50 s; 50–100 s; 100–125 s) was used to identify candidate earthquakes yielding high signal-to-noise ratio Rayleigh waves. The lower magnitude threshold was subsequently iteratively reduced to 5.1 to secure improved azimuthal earthquake illumination from the spreading ridges west and south of Australia. Of many hundreds of earthquakes screened, 142 were ultimately earmarked for tomography (Figure 2a).

For each of these earthquakes, the vertical-component seismograms were filtered into 13×10 mHz wide frequency bands with centre periods ranging from 20 to 167 s using a zero-phase-shift, four-pole Butterworth filter centred at the period of interest (Figure 2b). For each earthquake, a window was then manually defined at each period to isolate the fundamental mode Rayleigh waves from other seismic phases. The morphological similarity of teleseismic waveforms across an array was exploited to remove from consideration poor quality Rayleigh waves: at each period, only those Rayleigh waves from stations yielding cross correlation coefficients ≥ 0.8 against a 'template' Rayleigh wave from a high-quality station – typically a permanent Australian National Seismic Network station – were selected for further analysis. A final visual screening of all individual Rayleigh waves rectified a small percentage of waveforms we considered to have been erroneously included or discarded by the cross-correlation analysis.

Being predicated on the assumption of planar wave fronts, the validity of two-plane-wave tomography varies inversely with the geographic extent of a seismic array. As circumvention, we subdivided the expansive composite array into two sub-arrays approximately encompassing the northern and southern portions of the state of South Australia. In this scheme, a given earthquake is effectively treated as two separate earthquakes, both incident on the individual sub-arrays. A reference 1D Rayleigh wave phase velocity dispersion curve for southern Australia (Figure 2e) derived by merging 1D average curves for southern Australia (periods 3–20 s; O'Donnell et al., 2023) and continental Australia (periods 4–200 s; Magrini et al., 2023) provided starting values for the 2D two-plane-wave phase velocity inversions. Following Yang and Forsyth (2006a), finite frequency sensitivity kernels were used to represent the sensitivities of Rayleigh wave phases and amplitudes to structure. Trade-off analysis was used in the selection of optimal regularisation for the tomography; we concluded that a damping value of 0.4 and smoothing length scale of 70 km represented a good compromise between data fitting and model complexity (Figure 2f).

6 Rayleigh Wave Phase Velocity Maps

In the 2D two-plane-wave tomography, at each period the isotropic Rayleigh wave phase velocity variations best explaining the observed phase and amplitude variations between stations were inferred on a grid with a node spacing of 0.25° spanning southern Australia.

Figure 3 shows the inferred 2D Rayleigh wave phase velocity uncertainty, calculated from the covariance matrix, at a selection of periods. As expected, the uncertainty is least where the concentration of seismic stations is greatest and increases toward the model periphery. Superimposed is a trend of increasing uncertainty with increasing period because the lengthening wavelength of the Rayleigh waves decreases spatial resolution. Given the difficulty in quantifying the uncertainty of the antecedent seismograms, coupled with our adoption of a particular starting model and regularisation in the tomography, we emphasise that the inferred uncertainty has more meaning in a relative rather than absolute sense.

Companion Figure 4 shows the resolving capability of the inversion. As expected, the patterns mirror that of the phase velocity uncertainty maps: resolution is best where the concentration of seismic stations is greatest, and naturally degrades with increasing period as wavelengths lengthen. The latter is hastened by the progressively decreasing number of seismograms constraining the two-plane-wave tomography at periods >100 s (Figure 2d). Within the region enclosed by the red polygon, the resolution matrix indicates that the morphology and amplitude of velocity anomalies of length scale 1.5° and greater are faithfully imaged at 25 s period. At 125 s period, meanwhile, structure of length scale > 2° is resolved, albeit with more anomaly amplitude diminution and smearing relative to shorter periods.

Figure 5 shows the Rayleigh wave phase velocity maps inferred by two-plane wave tomography for a selection of periods. We defer discussion of structure to the more readily-interpretable shear wave velocity model.

7 Shear Wave Velocity Model

We next inverted the phase velocity maps to derive a pseudo 3D shear wave velocity model of southern Australia. The sensitivity of fundamental mode Rayleigh wave phase velocities to shear wave velocity structure (e.g., Figure 2c) facilitates the development of shear wave velocity models. To this end, we extracted a suite of 2253 'local' Rayleigh wave phase velocity dispersion curves from the 2D Rayleigh wave phase velocity maps by sampling the maps at regular geographic 0.2° grid in-

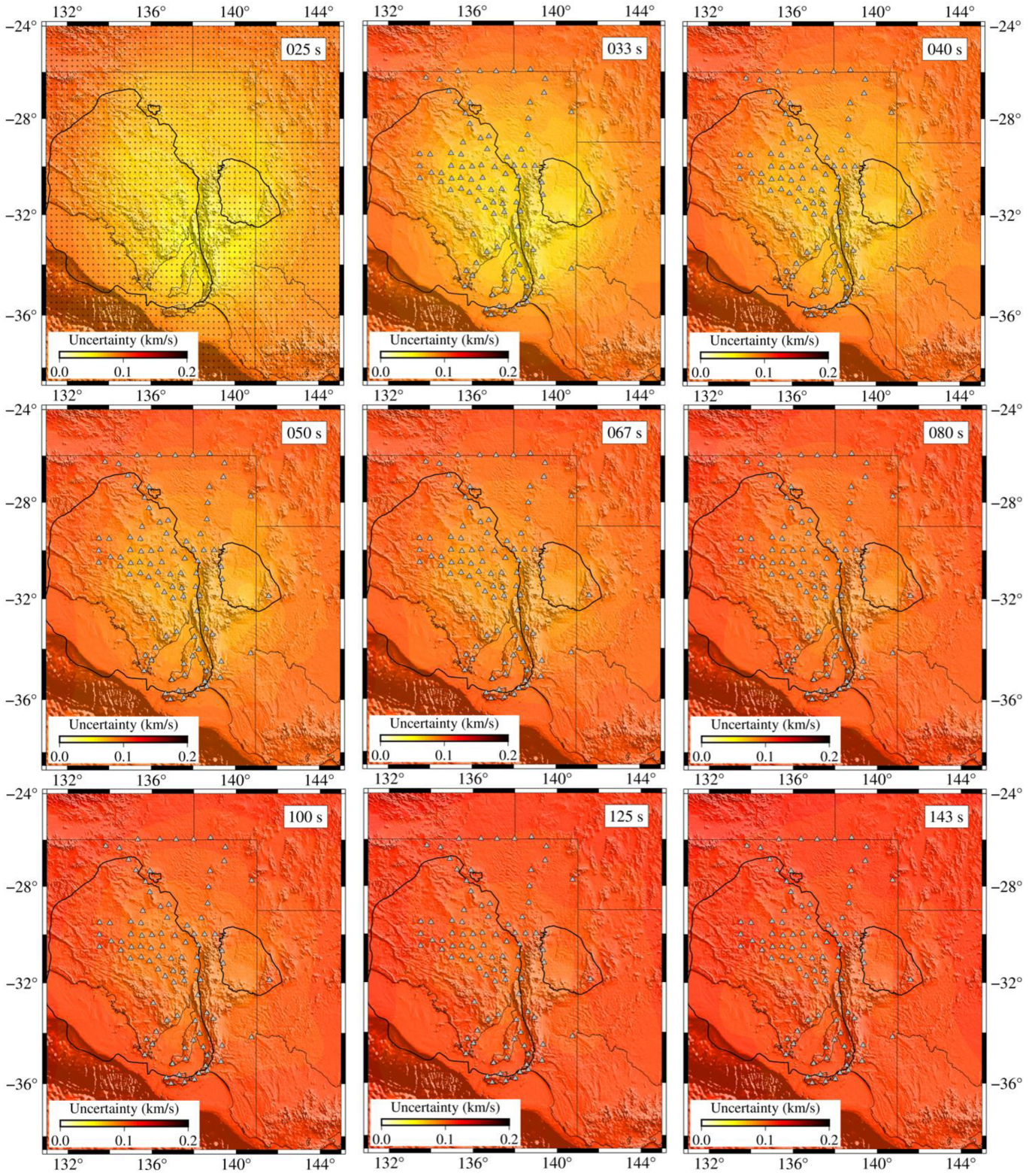

Figure 3 Rayleigh wave phase velocity model uncertainty at a selection of periods. The tomography grid node locations are superimposed on the 25 s map. Seismic station locations are shown as triangles on all other maps.

tervals. Each local dispersion curve was then inverted for 1D vertically-polarised shear wave velocity (V_{SV}) structure at the grid location, and the ensemble of 1D V_{SV} profiles combined to yield a pseudo 3D V_{SV} model of southern Australia to 250 km depth.

For each local dispersion curve, we used the Markov chain Monte Carlo transdimensional Bayesian search algorithm *Bayhunter* (Dreiling and Tilmann, 2019; Dreiling et al., 2020) to obtain a distribution of 1D V_{SV} profiles consistent with the dispersion data. The search space encompassed the depth range 0–400 km, a V_{SV} range of 2.8–5.5 km/s and a V_P/V_S range of 1.7–1.8, with the number of layers invoked to explain the dispersion data permitted to vary from 1–30, subject to a

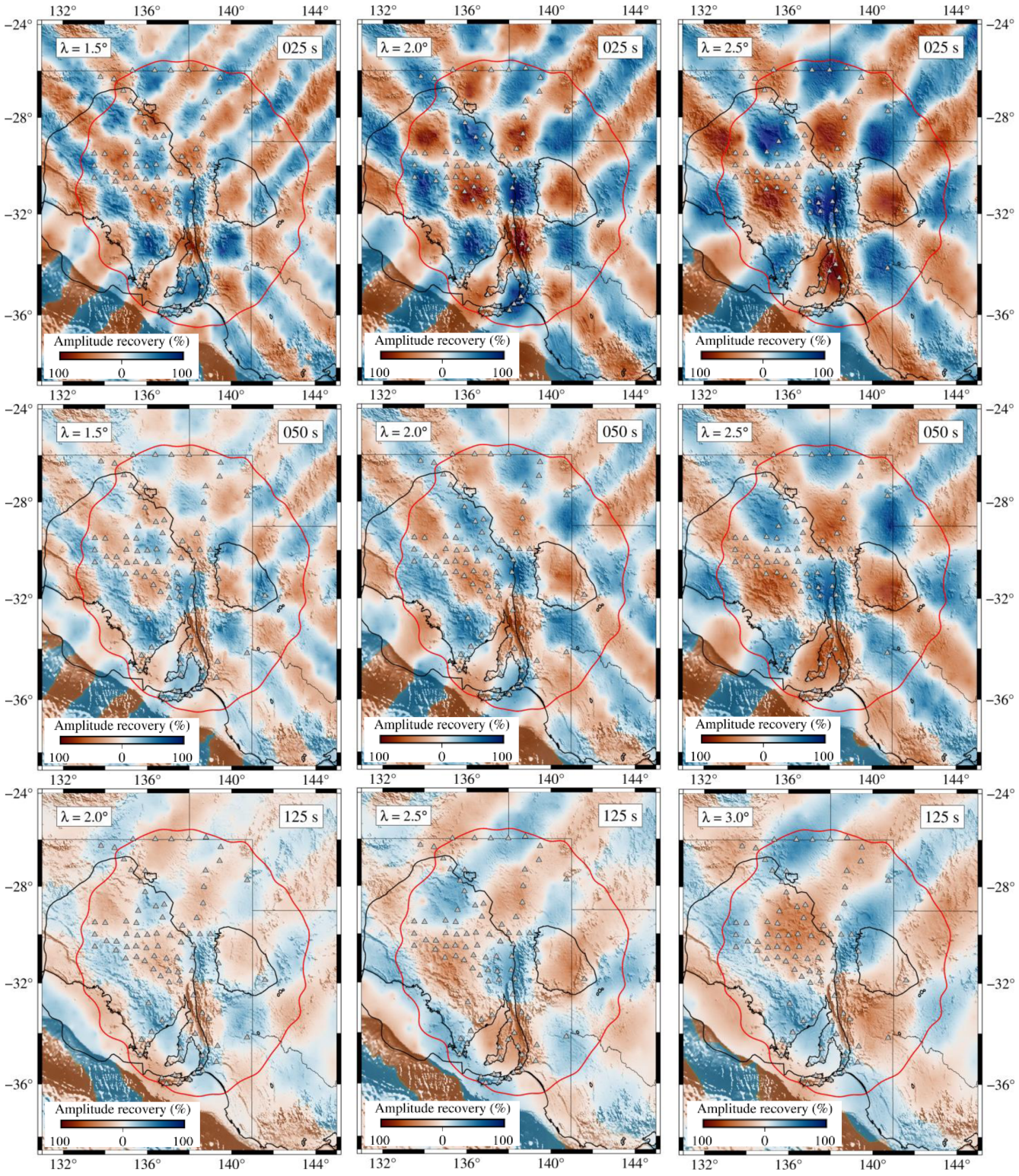

Figure 4 Rayleigh wave phase velocity model resolution at representative periods of 25 s (top row), 50 s (middle row) and 125 s (bottom row). We present the resolution matrix multiplied by checkerboard patterns of phase velocity anomalies of wavelength 1.5°, 2.0°, 2.5° and 3.0° plus random gaussian noise. 100% represents complete amplitude recovery of positive/negative velocity anomalies. Seismic station locations are shown as triangles. We confine our subsequent discussion of imaged structure to the region enclosed by the red polygon.

minimum layer thickness of 1 km. Moho depths were initialised to be within ± 5 km of the Australian Moho model (Kennett et al., 2023), but the algorithm was free to subsequently explore values outside this range. For each proposed 1D V_{SV} model, the corresponding dispersion curve was calculated using the *Computer Programs in Seismology* routine *SURF96* (Herrmann, 2013).

To ensure broad exploration of the model space, we ran the Monte Carlo search for 300,000 iterations and 100 independent chains. The first 200,000 iterations

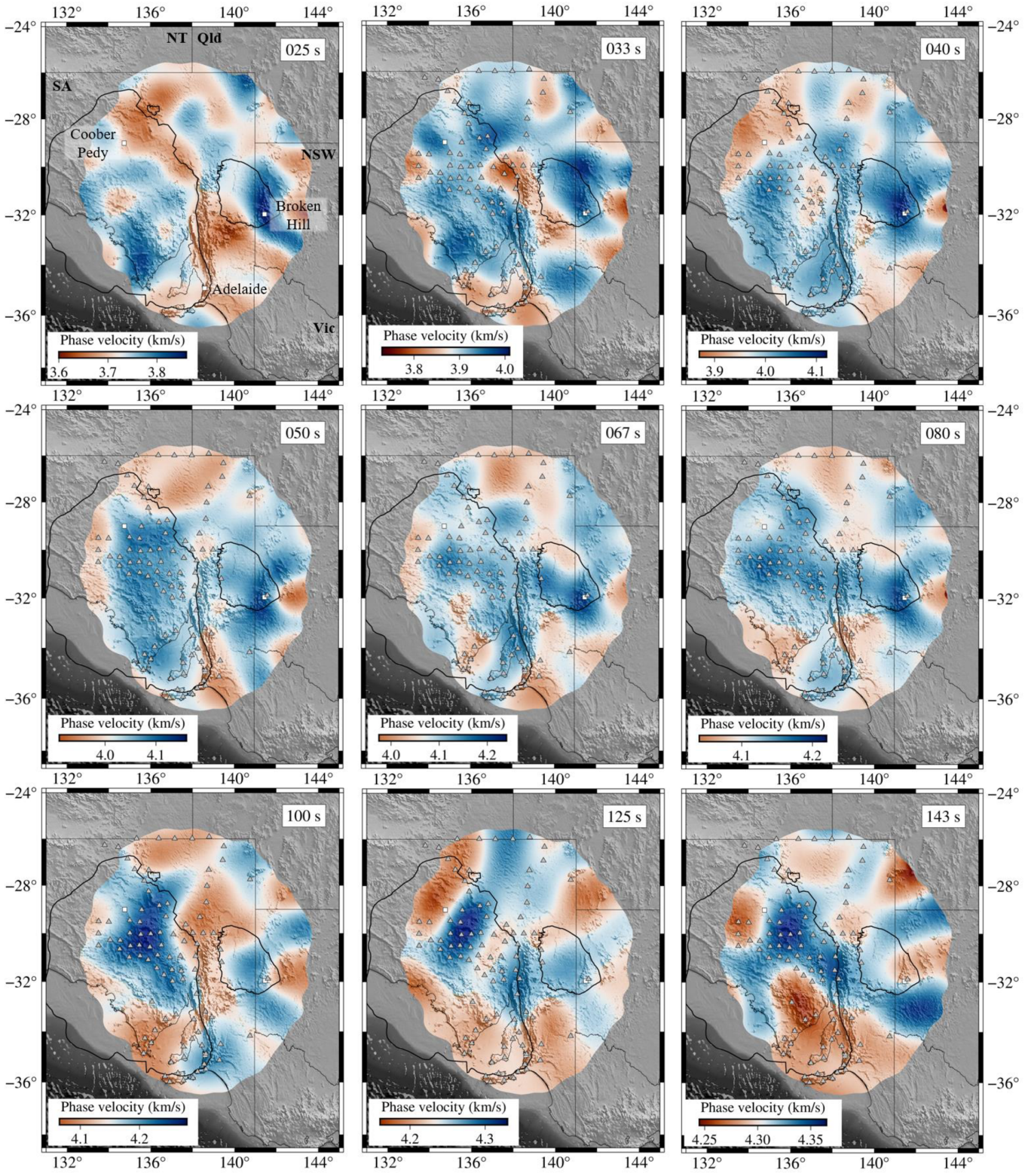

Figure 5 Rayleigh wave phase velocity model at a range of periods. Tailored scale bars are used at each period to emphasise lateral velocity variations. Regions of higher uncertainty and lower resolution are masked. Seismic station locations are shown as triangles.

were discarded as burn-in with the remaining 100,000 constituting the exploration phase. Chains which failed to converge were declared outliers and discarded. Each final 1D posterior V_{SV} distribution was built from 10,000 models of the exploration phase sub-sampled from all non-outlier chains. Figure 6 shows inferred V_{SV} profiles for grid node locations in the vicinity of Tunkillia gold deposit in the central Gawler Craton; Olympic Dam IOCG-deposit in the Olympic Cu–Au Province along the eastern Gawler Graton; Hillside IOCG-deposit at the southern end of the Olympic Cu–Au Province; and Broken Hill in the Curnamona Province.

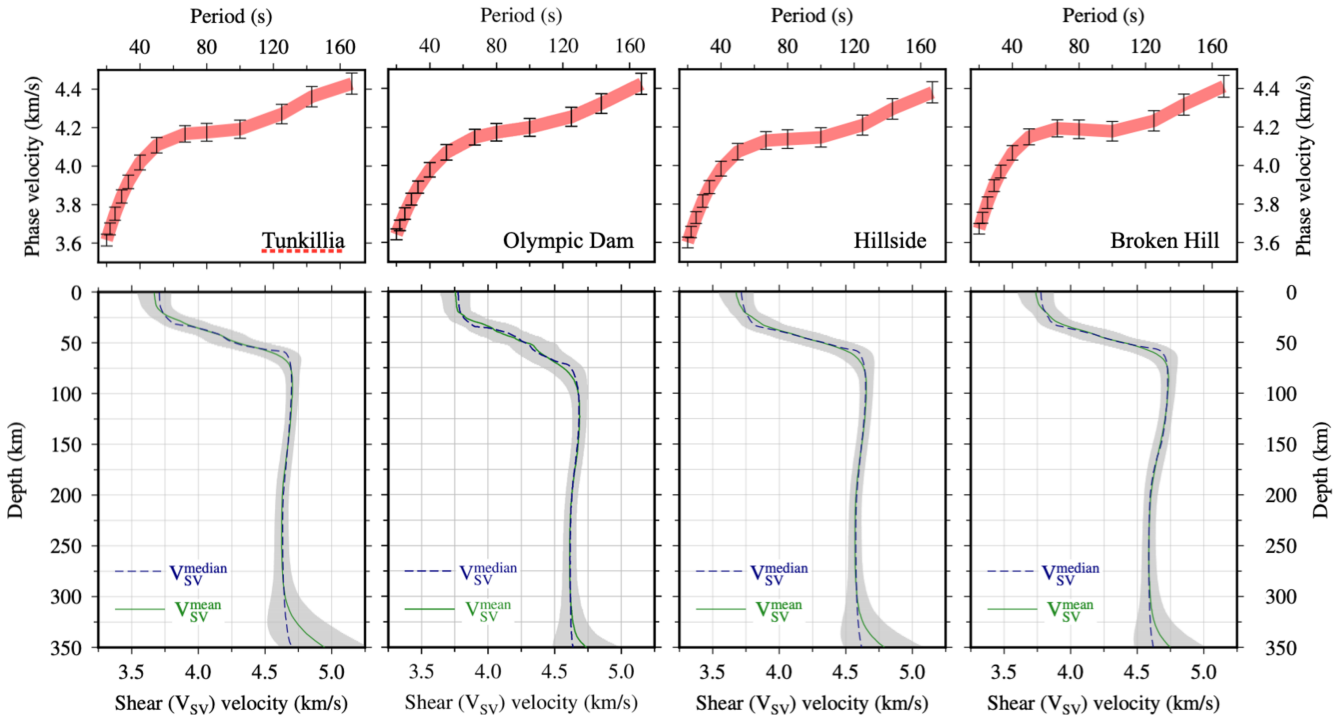

Figure 6 Observed and modelled Rayleigh wave phase velocity dispersion curves (top) and corresponding inferred vertically-polarised shear wave velocity V_{SV} profiles (bottom) for Tunkillia gold deposit in the Central Gawler Craton Gold Province; Olympic Dam IOCG-deposit in the Olympic Cu–Au Province at the eastern Gawler Graton margin; Hillside IOCG-deposit at the southern end of the Olympic Cu–Au Province; and Broken Hill in the Curnamona Province (see Figures 1, 7 and 8 for locations). In the V_{SV} profiles, the solid green line is the mean of the posterior V_{SV} distribution; the dashed blue line is the median; and the grey area outlines lower and upper standard deviation bounds. Note the slight perturbation in uppermost mantle V_{SV} structure for the node in the vicinity of Olympic Dam. Upper-to-mid crustal structure is not well constrained by our phase velocity period range and should not be interpreted.

Of the 2253 grid nodes, we discarded 12 for which the search failed to converge. The ensemble of 2241 inferred 1D V_{SV} profiles were gridded to generate a pseudo 3D V_{SV} model of southern Australia to 250 km depth. Figures 7 and 8 show horizontal slices through the model at a range of depths from 30 to 225 km. Figure 9 shows vertical slices along six profiles.

8 Discussion

8.1 The Moho

Accurately mapping the Moho using surface waves alone can be challenging because of the trade-off between Moho depth and crust and mantle shear wave velocities, especially in the absence of prior and/or independent constraining information (e.g., Lebedev et al., 2013). We determined that our iso-velocity $V_{SV} = 4.1$ km/s surface yielded a maximum concordance with the ensemble of data contributing to the latest iteration of the Australian Moho model (Kennett et al., 2023), and hence adopted this iso-velocity surface as diagnostic of the Moho (Figure 7). The Moho model is characterised by depths in the ∼40–45 km range, with ∼40 km thick crust underlying the inferred core of the South Australian Craton. However, we acknowledge some significant deviations from, for instance, individual receiver function inferences, and refer the reader to Agrawal et al. (2023) and Kennett et al. (2023) for more detailed consideration of crustal thickness across South Australia. We next examine lithospheric mantle structure.

8.2 The lithospheric mantle seismic structure of the South Australian Craton

AK135 Earth model (Kennett et al., 1995) isotropic shear wave velocities are ∼4.5 km/s at lithospheric mantle depths. Shear wave velocities elevated beyond this are considered characteristic of geochemically-depleted, cold cratonic lithosphere (e.g., Eaton et al., 2009, and references therein), with iso-velocity surfaces defined by percentage perturbations above reference models

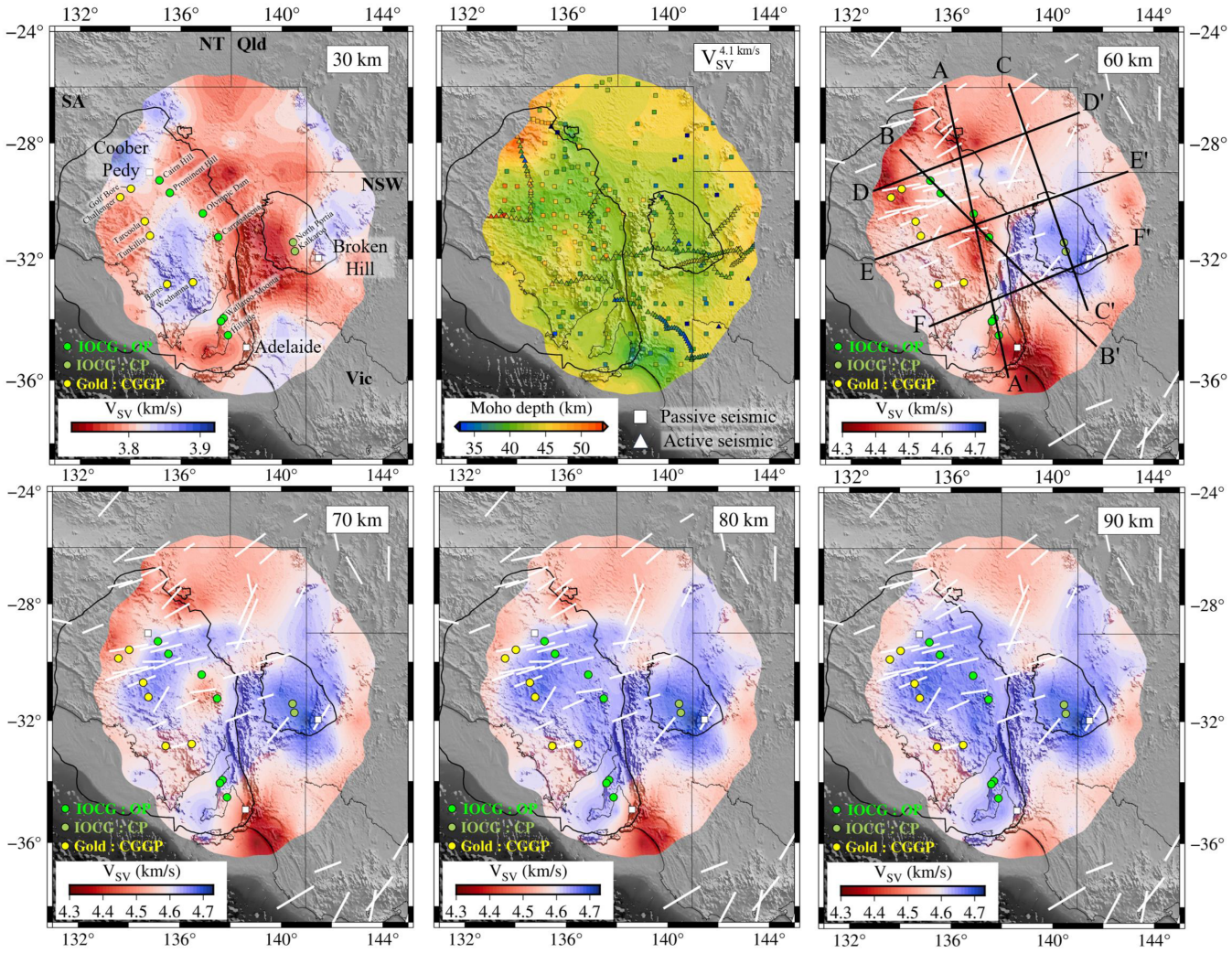

Figure 7 Horizontal slices through the pseudo 3D vertically-polarised shear wave velocity (V_{SV}) model of southern Australia at depths 30-90 km. Lime green dots show the locations of significant IOCG deposits of the Olympic Cu–Au Province (OP); olive green dots show the locations of significant IOCG deposits of the Curnamona Province (CP); yellow dots show the locations of significant gold deposits of the Central Gawler Gold Province (CGGP). A reduced V_{SV} scale bar at 30 km depth captures subtle intra-crustal velocity variations. We use the iso-velocity $V_{SV} = 4.1$ km/s surface as diagnostic of the Moho because this value yields a maximum concordance with the ensemble of data (superimposed symbols) contributing to the latest iteration of the Australian Moho model (Kennett et al., 2023). We interpret $V_{SV} \geq 4.6$ km/s as characterising cratonic core lithosphere. White lines show fast polarisation directions of inferred upper mantle seismic anisotropy deduced by shear wave splitting analyses (Eakin et al., 2021, 2023). The locations of the vertical profiles of Figure 9 are superimposed on the 60 km depth slice. As in the antecedent Rayleigh wave phase velocity maps, regions of higher uncertainty and lower resolution are masked.

(e.g., +1–2%; Simons and van der Hilst, 2002) or absolute velocity values (e.g., 4.6 km/s; Li and Burke, 2006) often invoked as seismic proxies of cratonic lithosphere.

Given the suite of parameterisation and regularisation choices that cumulatively influence the two-plane-wave tomography and subsequent V_{SV} model development (described as "*all the little choices*" by Fichtner et al., 2025), we emphasise that relative velocity variations are better constrained than are absolute values. Accordingly, while we here interpret V_{SV} of ∼4.6 km/s (equivalent to ∼2% above isotropic AK135 values) and higher as characterising cratonic core lithosphere, and V_{SV} of ∼4.55–4.60 km/s (equivalent to ∼AK135 +1% < V_{SV} < ∼AK135 +2%) as characterising cratonic margin lithosphere, it is the relative V_{SV} variations and spatial patterns that primarily inform our interpretation.

Using this proxy of elevated shear wave velocities, the core of the South Australian Craton begins to reveal itself from ∼60 km depth in Figures 7, 8 and 9. Between 80 and 150 km depth, the core evidently comprises the lithosphere underlying the eastern Gawler Craton, Curnamona Province, and intervening Northern Flinders Ranges/Adelaide Superbasin. The V_{SV} model suggests that at these depths, cratonic lithosphere extends southward and northeastward well beyond the conventionally-defined boundary of the Curnamona Province. Admittedly, this may be partially attributable to anomaly smearing (see Figure 4). At depths greater than 150 km, the cratonic keel is restricted to the eastern Gawler Craton and southern Curnamona Province, with a diminishing but lingering hint of elevated V_{SV} in the vicinity of Adelaide and the Barossa

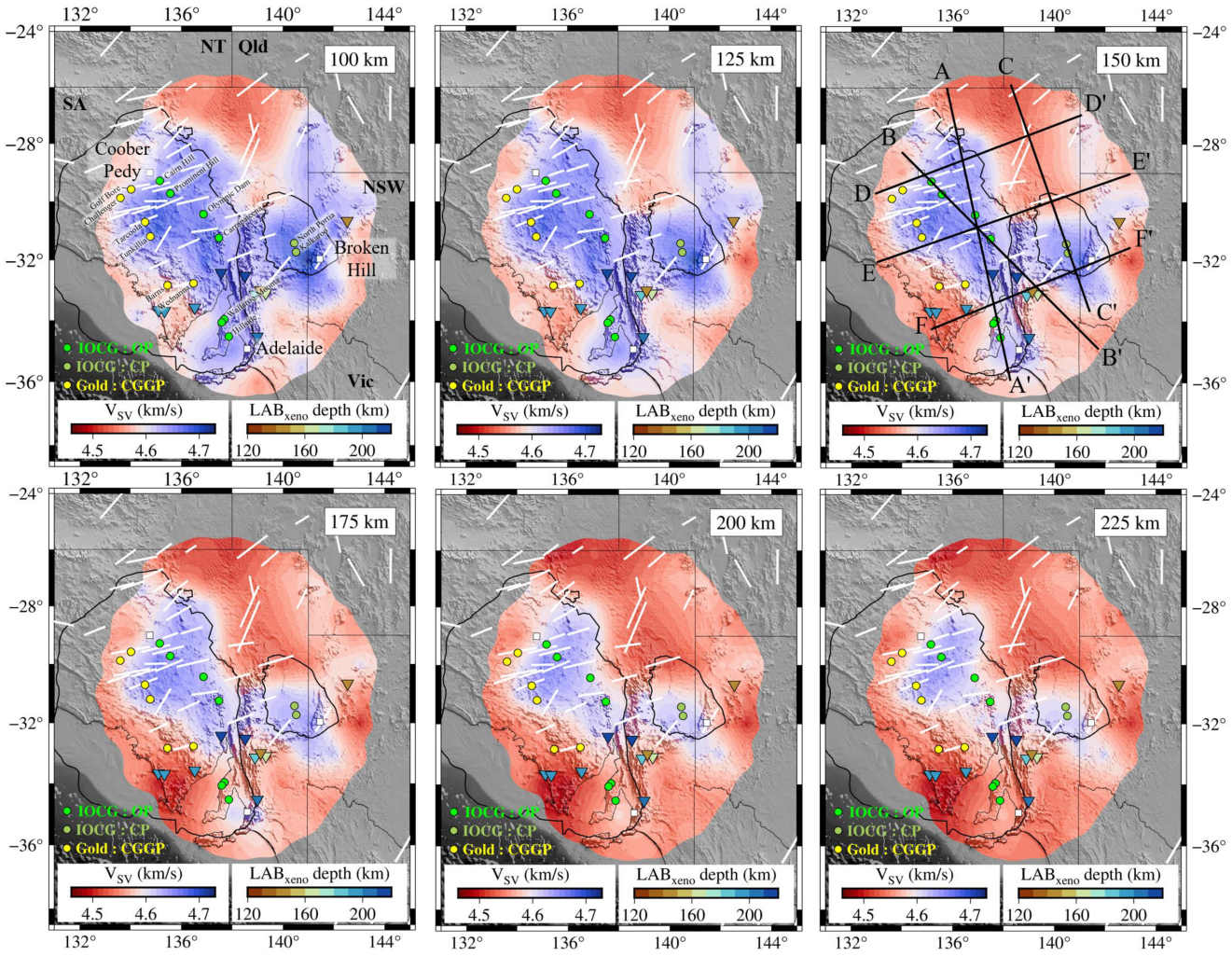

Figure 8 Horizontal slices through the pseudo 3D vertically-polarised shear wave velocity (V_{SV}) model of southern Australia at depths 100-225 km. Lime green dots show the locations of significant IOCG deposits of the Olympic Cu–Au Province (OP); olive green dots show the locations of significant IOCG deposits of the Curnamona Province (CP); yellow dots show the locations of significant gold deposits of the Central Gawler Gold Province (CGGP). Colour-coded triangles show lithosphere-asthenosphere boundary (LAB) depths as inferred by xenocryst analyses (Sudholz et al., 2022, and references therein). White lines show fast polarisation directions of inferred upper mantle seismic anisotropy deduced by shear wave splitting analyses (Eakin et al., 2021, 2023). We interpret $V_{SV} \geq 4.6$ km/s as characterising cratonic core lithosphere. The locations of the vertical profiles of Figure 9 are superimposed on the 150 km depth slice. Regions of higher uncertainty and lower resolution are masked.

Complex at the southeastern margin of the Gawler Craton (see Figure 1 for Barossa Complex location).

The tomographically-inferred lithospheric mantle 'footprint' of the South Australian Craton is generally consistent with fast polarisation directions (white lines in Figures 7 and 8) inferred by shear wave splitting analyses (Eakin et al., 2021, 2023). The pervasive ENE–WSW aligned fast directions have been interpreted as the preserved fossil signature of lithospheric mantle deformation developed during cratonisation of the South Australian Craton (Eakin et al., 2023). A notable deviation from the predominant ENE–WSW aligned fast directions occurs for the Kati Thanda–Lake Eyre Basin in northeastern South Australia, where fast directions are more aligned with NNE-directed absolute plate motion. Eakin et al. (2023) suggest that this is rooted in an enhanced contribution from asthenospheric anisotropy and, by implication, younger, thinner lithosphere. This inference is consistent with the contrasting shear wave velocity structure we image between the eastern Gawler Craton and adjacent Kati Thanda–Lake Eyre Basin (Figures 7, 8 and 9).

8.3 Comparison with mantle xenolith, electrical resistivity and Sm–Nd isotope data

Figure 10 compares our mantle V_{SV} structure with (i) mantle electrical resistivity structure inferred from MT data (Thiel et al., 2016) and (ii) two-stage depleted mantle model ages (T_{DM2}) for felsic and mafic-to-intermediate rocks inferred from Sm–Nd isotopic data (Wade et al., 2024). The two-stage depleted mantle model age marks the time at which crustal material – in this case felsic and mafic-to-intermediate rock – was extracted from the mantle. For instance, an Archean mantle model age implies that the lithosphere has ex-

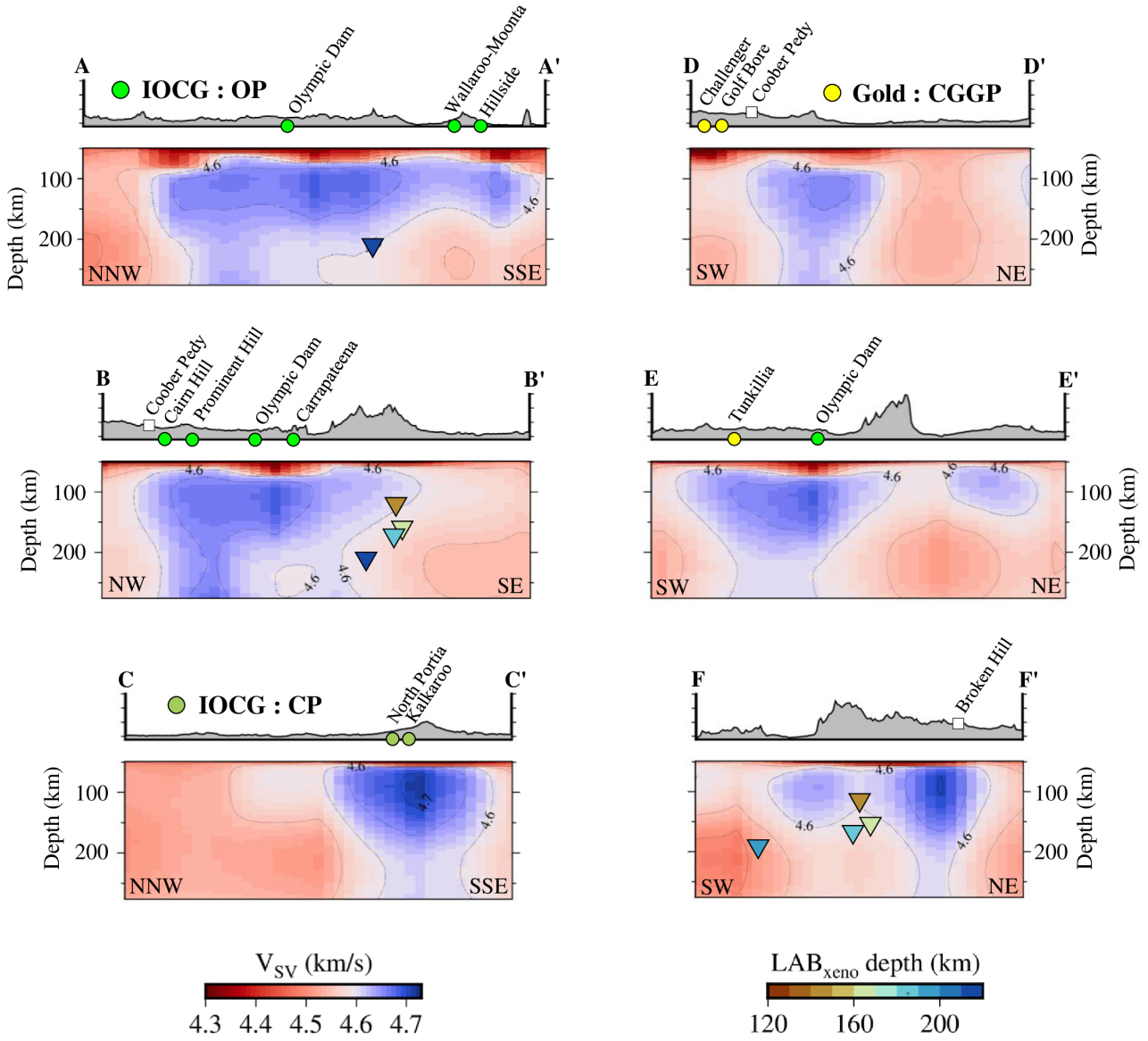

Figure 9 Vertical slices through the pseudo 3D vertically-polarised shear wave velocity (V_{SV}) model of southern Australia along the profiles shown in Figures 7 and 8. Lime green dots show the locations of significant IOCG deposits of the Olympic Cu–Au Province (OP); olive green dots show the locations of significant IOCG deposits of the Curnamona Province (CP); yellow dots show the locations of significant gold deposits of the Central Gawler Gold Province (CGGP). Colour-coded triangles show lithosphere-asthenosphere boundary (LAB) depths as inferred by xenocryst analyses (Sudholz et al., 2022, and references therein). Even though seismically- and petrologically-defined lithospheric thicknesses need not coincide (e.g., Eaton et al., 2009), spatial variations in the petrologically-defined lithospheric thickness across the South Australian Craton are generally coherent with our V_{SV} model, with the petrologically-defined lithosphere-asthenosphere boundary approximately coinciding with the deepest occurrence of the 4.6 km/s V_{SV} contour across most data points.

isted since the Archean and that the dominant events that extracted melts from the mantle occurred in the Archean. MT is a passive electromagnetic technique that images Earth electrical resistivity and is a complementary technique to seismic tomography for investigating the lithospheric mantle. Both methods are sensitive to temperature, but in terms of composition, seismic velocities are more sensitive to bulk rock chemistry, and particularly the Fe/Mg ratio, while MT resistivities are more sensitive to minor conductive phases such as graphite, sulfides, or phlogopite and the water content of nominally anhydrous minerals like olivine and pyroxene (e.g., Selway, 2013). MT is therefore more sensitive to rocks that have experienced small degrees of partial melting and fluid-rich metasomatism, while seismic models are more reflective of mantle age and bulk melting.

8.3.1 The Gawler Craton core

The central core of the Gawler Craton, from approximately the northern Eyre Peninsula to the Karari Shear Zone (see Figure 1 for locations), displays characteristics typical of thick, depleted, Archean lithosphere in all datasets (Figure 10). Shear wave velocities are high (V_{SV}

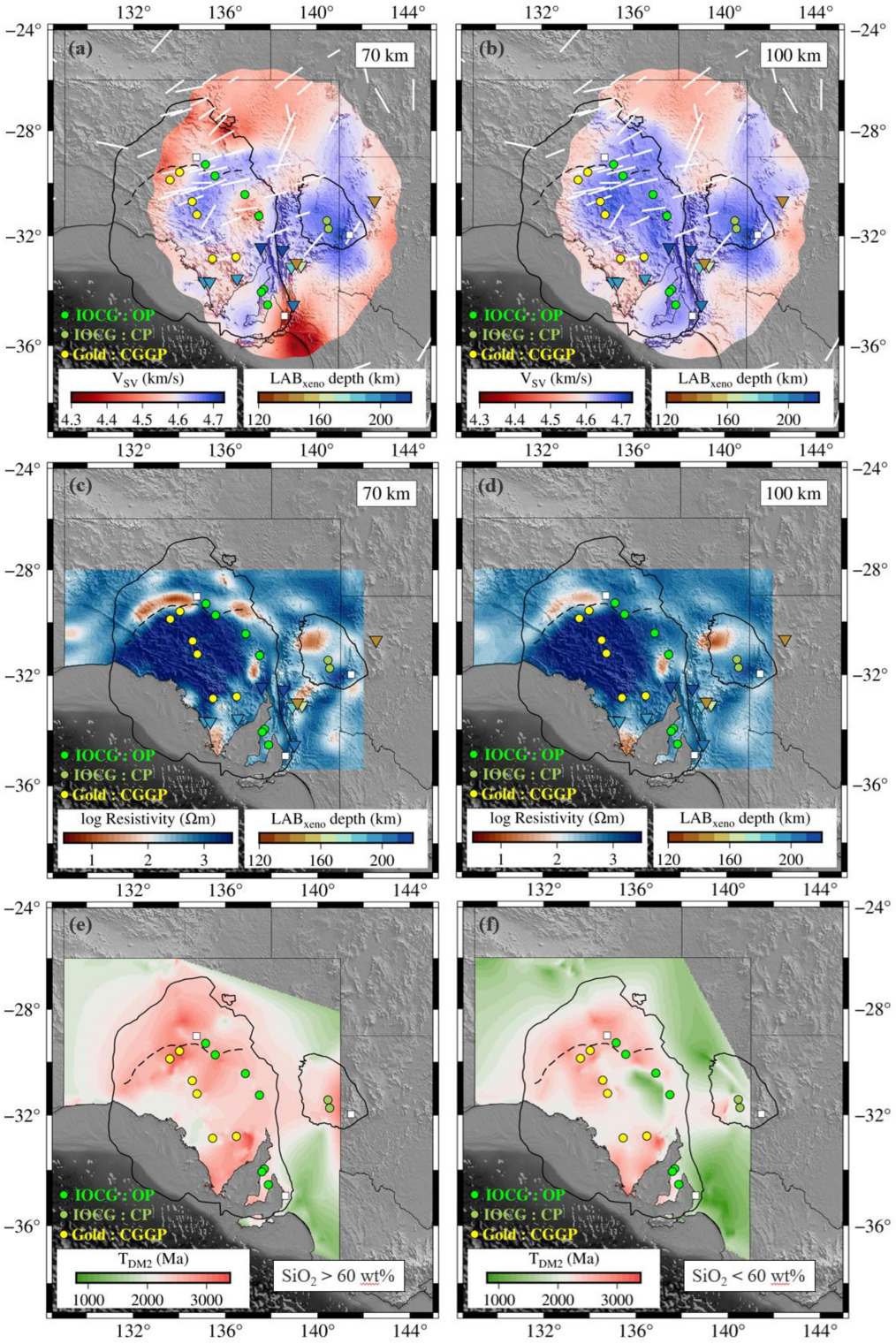

Figure 10 (a) and (b) Horizontal slices through the vertically-polarised shear wave velocity (V_{SV}) model of southern Australia at depths 70 and 100 km. We interpret $V_{SV} \geq 4.6$ km/s as characterising cratonic core lithosphere; (c) and (d) horizontal slices through the electrical resistivity model of southern Australia developed from MT data (Thiel et al., 2016) at depths 70 and 100 km; (e) and (f) two-stage depleted mantle model ages (T_{DM2}) for felsic and mafic-to-intermediate rocks, respectively, inferred from Sm-Nd isotopic data (Wade et al., 2024). White lines show fast polarisation directions of inferred upper mantle seismic anisotropy deduced by shear wave splitting analyses (Eakin et al., 2021, 2023). The dashed line is the Karari Shear Zone. Lime green dots show the locations of significant IOCG deposits of the Olympic Cu–Au Province (OP); olive green dots show the locations of significant IOCG deposits of the Curnamona Province (CP); yellow dots show the locations of significant gold deposits of the Central Gawler Gold Province (CGGP). Colour-coded triangles show lithosphere-asthenosphere boundary (LAB) depths as inferred by xenocryst analyses (Sudholz et al., 2022, and references therein).

> ∼4.6 km/s), consistent with cool lithospheric mantle temperatures and compositions that are depleted in Fe. Lithospheric thicknesses from petrological analysis of kimberlite-hosted mantle xenocrysts (Sudholz et al., 2022, and references therein) approach and exceed 200 km and are coherent with our V_{SV} model (Figures 8 and 9). Electrical resistivities are high, consistent with thick lithosphere, cool temperatures, and dehydrated and depleted compositions. Both felsic and mafic-to-intermediate two-stage depleted mantle model ages are dominantly > 2500 Ma, consistent with lithospheric mantle that experienced major melting events in the Palaeoproterozoic to Archean and has been stable since that time. There is a much younger (∼1000 Ma) band of mafic-to-intermediate mantle model ages just southwest of the Olympic Dam and Carrapateena IOCG deposits, which may be associated with the ca. 820–830 Ma Gairdner Dolerite, and both felsic and mafic-to-intermediate mantle model ages are ∼2000 Ma on the northwest Eyre Peninsula coast, coincident with the ca. 1608–1633 Ma St Peter Suite, with potentially correlative lower velocities in the V_{SV} model.

8.3.2 The Curnamona Province

The Curnamona Province likewise displays relatively consistent patterns between the datasets. Shear wave velocities are high and consistent with thick, depleted lithosphere through most of the province, except for lower velocities that extend from the northernmost tip of the province northward beneath the Lake Eyre Basin. Electrical resistivity is moderate to high through most of the province except for a low resistivity zone in the northwest. There is an offset between the low resistivity zone and the low shear wave velocity zone, which could be a function of model resolution. The felsic mantle model ages show a very similar pattern to the Curnamona Province V_{SV} model, with elevated shear wave velocities tracking older (> 2500 Ma) ages through most of the province, and lower velocities at the northern tip of the province and underlying the Lake Eyre Basin corresponding with younger (< 2000 Ma) ages. The mafic-to-intermediate model age map in the Curnamona Province suffers from the difficulties of gridding sparse data.

8.3.3 The western and northern Gawler Craton margins

At the western and northern margins of the Gawler Craton, all datasets suggest a transition away from thick, cratonic core lithosphere, although the location of this transition differs slightly between datasets. In the seismic V_{SV} model, from depths of 70 to > 200 km, velocities show a marked decrease from the central core of the craton to the west and northwestern parts of the model. This decrease is approximately parallel to, but substantially inboard of, the conventionally-defined margin of the Gawler Craton (Figure 8). In the MT model, resistivities sharply decrease along a trend approximately coincident with the Karari Shear Zone, which separates Archean rocks of the Mulgathing Complex to the south from Palaeoproterozoic rocks to the north, and bulk lithospheric mantle resistivities are lower to the north and west of this margin than in the central core of the craton (Figure 10). Pollett et al. (2019) jointly interpreted heat flow measurements and a 2D MT profile to place the northern margin of the Gawler Craton inboard of, but relatively close to, the conventionally-defined margin. Both mafic and felsic model ages show a distinct transition from ages > 2000 Ma on the craton to ages < 2000 Ma to the north and west of the craton, with the boundary approximately coincident with the conventionally-defined margin of the craton. Combined, these datasets all suggest a transition from cratonic core to cratonic margin lithospheric mantle. Hartnady et al. (2020) use Hf isotope compositions of zircons to suggest that the Coompana Province represents part of a Palaeoproterozoic-Mesoproterozoic arc system formed through hyper-extension of the western margin of the Archean Gawler Craton. This could conceivably explain the transition to lower seismic velocities, and by inference, thinner lithosphere, that we model in the western Gawler Craton. The offset between the isotopic edge of the craton and the gradient in seismic velocities should be a topic of further analysis. It is possible that the signature of the Proterozoic tectonism extends further east in the mantle than in the crust. However, given that the seismic coverage does not extend to the western margin of the craton and that there is likely to be northwest trending smearing of seismic features at these depths (Figure 4), this apparent discrepancy would be best investigated by the collection of more seismic data.

8.3.4 Thinner lithosphere beneath the southern Eyre Peninsula

The southern Eyre Peninsula has distinctly different characteristics in the geophysical and isotopic models. In the seismic V_{SV} model, velocities are lower than in the cratonic core from depths of 70 km to the base of the model. This notable absence of elevated shear wave velocities – and by inference, cratonic core lithosphere – at lithospheric mantle depths beneath the southern Eyre Peninsula (Figures 7 and 8) was similarly commented upon by de Laat et al. (2023) in their recently published tomography model of the Australian plate. The MT model likewise displays anomalously low resistivities in the lithospheric mantle of the southern Eyre Peninsula, although the low resistivities do not extend as far inland as the lower seismic velocities. Resistive mantle lithosphere beneath the northern Eyre peninsula is also suggested by a 200 km high-resolution MT profile (Curtis and Thiel, 2019). In contrast, both the felsic and mafic model ages are > 2500 Ma in the southern Eyre Peninsula. Mantle xenocrysts, meanwhile, from the central Eyre Peninsula suggest a petrological lithospheric thickness of ∼190–205 km (Sudholz et al., 2022), seemingly at odds with the spatially coincident low V_{SV} zone (Figures 8 and 10). A possible explanation might be stretching and metasomatism of the now southern Eyre Peninsula lithosphere during the Jurassic–Cretaceous separation of Australia and Antarctica, with the mantle xenocrysts hosted in the Jurassic kimberlites captur-

ing the pre-separation state of the lithosphere. The rifting event did not generate any magmatism in the Eyre Peninsula, so the model ages are unaffected by it, but it thinned and possibly metasomatised the mantle lithosphere, leading to the present-day seismically slower and electrically conductive mantle geophysical characteristics. Thinned lithosphere beneath coastal tracts of Wilkes Land in East Antarctica – the conjugate Gondwana margin – has been inferred in recent Antarctic seismic tomography studies (Chua and Lebedev, 2025; Hansen and Emry, 2025; Lloyd et al., 2020a).

8.3.5 The lithosphere between the Gawler Craton and Curnamona Province

The section of lithosphere between the Gawler Craton and Curnamona Province is seismically fast with characteristics indistinguishable from the cores of the Gawler Craton and Curnamona Province. Although a narrow region, our phase velocity resolution analysis at 50 s (primarily sensitive to upper lithospheric mantle depths) indicates that structure of wavelength comparable to the dimension of the separation can be resolved (Figure 4). The electrical resistivities are also moderate to high, and mantle model ages are generally > 2500 Ma, although the latter are not well constrained in this region (Wade et al., 2024). On the other hand, Rawlinson et al. (2016) suggest that there is no evidence in the lithospheric mantle that the Gawler Craton and Curnamona Province are currently connected based on a teleseismic relative arrival time body wave tomography developed using the WOMBAT data.

The seismic velocities characteristic of cratonic lithosphere that we infer are perhaps geologically surprising given that this section of lithosphere rifted during the breakup of Rodinia and therefore may be expected to have been thinned and metasomatised leading to lower velocities. The rifting was significant; the present-day total thickness of Adelaide Superbasin sediments that were deposited in the rift basin between the Gawler Craton and Curnamona Province exceeds 10 km in places, in addition to several kilometers of underlying rift-related mafic volcanics (Preiss et al., 2010). Further south, at the present-day southeastern margin of the Gawler Craton, the rifting proceeded to passive margin stage (Preiss, 2000), and in this location the seismic velocities are much lower and consistent with thinner lithosphere. Lithospheric thicknesses from mantle xenocrysts (Sudholz et al., 2022) show a pattern remarkably similar to the seismic V_{SV} model (Figures 8 and 9). The petrological lithospheric thickness at Eurelia, in the Adelaide Superbasin between the Gawler and Curnamona cratons, is estimated to be 210–220 km, while less than 100 km to the southeast in the Terowie cluster, petrological lithospheric thicknesses are estimated at 140–190 km (Figure 9). These datasets therefore suggest that the lithosphere did not thin significantly between the Gawler Craton and Curnamona Craton, even though the rifting event was significant, and that there is a steep gradient in lithospheric thickness at latitude ∼33°S.

8.4 A lithospheric seismic signature of IOCG deposits

Skirrow et al. (2018) concluded that IOCG deposits in the Olympic Dam region reside above the margin of a fertile and metasomatised lithospheric mantle zone located at depths exceeding 100 km. Inference of this zone was partially based on the mantle component of the Australian Seismological Reference Model (AuSREM; Kennett et al., 2012) that Skirrow et al. (2018) relied upon to constrain the regional lithospheric mantle seismic structure. However, the AuSREM model has since been superseded by higher resolution models developed using newly acquired data. This likely explains our contrasting conclusion, that the most significant known IOCG deposits of the Olympic Cu–Au metallogenic Province (e.g., Olympic Dam, Carrapateena, Hillside) reside above, or proximal to, a seismically slow uppermost lithospheric mantle layer (depths shallower than ∼75 km) underlain by the electrically resistive and seismically fastest lithospheric mantle in the region (Figures 7, 8 and 9).

The eastern Gawler Craton margin has long been associated with an adjacent band of anomalously electrically conductive lithospheric mantle inferred by magnetotelluric data (Thiel et al., 2016; Selway et al., 2024). Magnetotelluric (Heinson et al., 2006), seismic reflection (e.g., Heinson et al., 2018; Wise and Thiel, 2020), and seismic ambient noise data (O'Donnell et al., 2023) image zones of coincident low electrical resistivity, low seismic reflectivity, and low shear wave velocities in the mid-to-lower crust underlying or adjacent to Olympic Province IOCG deposits. Our 30 km depth slice in Figure 7 is similarly consistent with the inference that the Olympic Dam and Carrapateena IOCG deposits reside above the western margin of a low shear wave velocity zone in the mid-crust (O'Donnell et al., 2023). Previous authors have suggested these various geophysical data express metalliferous fluid pathways from mantle and lower-crustal reservoirs through the mid-to-upper crust (e.g., Heinson et al., 2006, 2018; Wise and Thiel, 2020; O'Donnell et al., 2023). The North Portia and Kalkaroo IOCG deposits of the Curnamona Province similarly reside above, or are proximal to, notably seismically fast lithospheric mantle (Figures 7, 8 and 9). While a seismically slow uppermost lithospheric mantle layer is not apparent beneath North Portia and Kalkaroo, they do, like Olympic Domain counterparts, overlie a low shear wave velocity zone in the mid-to-lower crust (see 30 km depth slice in Figure 7 and O'Donnell et al., 2023).

IOCG-formation models reference melting of primed, metal-enriched metasomatised lithospheric mantle (e.g., Groves et al., 2010; Skirrow, 2022; Groves and Santosh, 2023). Based on the geochemical and isotopic composition of mafic intrusive rocks of the Gawler Range Volcanics and Hiltaba Suite, Wade et al. (2019) argue that the Gawler Craton lithospheric mantle was metasomatised and primed by earlier subduction events, possibly as early as the Neoarchean. Our seismic V_{SV} model points to particularly cool, thick, iron-depleted lithospheric mantle underlying major IOCG deposits of the Olympic Cu–Au Province and

Curnamona Province. This in turn suggests partial melting of the precursor lithospheric mantle – leaving the iron-depleted husk – with the melt products migrating upward to fertilise the uppermost mantle and/or lower crust according to accessible fluid pathways. While our seismic model cannot discriminate between candidate geodynamic triggers, recent geochemical and geochronological analyses suggest that the magmatism and hydrothermal activity associated with the 1.6 Ga Olympic mineralisation event is best explained by plume impact (e.g., Wade et al., 2022b,a; Jagodzinski et al., 2023). As suggested by Groves et al. (2010) and evidenced here, preservation of the IOCG deposits was facilitated by their formation above buoyant, iron-depleted lithospheric mantle.

9 Conclusions

Using teleseismic Rayleigh waves from 142 earthquakes recorded on three recent temporary broadband seismic arrays in southern Australia, we have developed a vertically-polarised shear wave velocity (V_{SV}) model of the South Australian Craton from the lower crust to 250 km depth.

Adopting $V_{SV} \geq 4.6$ km/s (equivalent to ∼AK135 +2%) as a proxy for cratonic core lithospheric mantle, and V_{SV} of ∼4.55-4.60 km/s (equivalent to ∼AK135 +1% < V_{SV} < ∼AK135 +2%) as characterising cratonic margin lithosphere, for depths ∼75–150 km, our model suggests that the 'footprint' of cratonic core lithosphere (i) encompasses the eastern Gawler Craton, Curnamona Province – plus southward and northeastward beyond the conventionally-defined province boundary – and intervening Adelaide Superbasin north of ∼33°S; (ii) terminates approximately parallel to, but substantially inboard of, the conventionally-defined western margin of the Gawler Craton; and (iii) is absent for the southern Eyre Peninsula. At depths exceeding 150 km, the seismic expression of the cratonic keel becomes ever more restricted to the eastern Gawler Craton – including a signature in the vicinity of the Barossa Complex at the southeastern Gawler Craton margin – and southern Curnamona Province.

We glean further insight by comparing the seismic model with mantle xenocryst data, two-stage depleted mantle model ages for felsic and mafic-to-intermediate rocks inferred from Sm–Nd isotopic data, and 3D mantle resistivity structure modelled using magnetotelluric data.

The central core of the Gawler Craton, from approximately northern Eyre Peninsula to the Karari Shear Zone, displays characteristics typical of thick, depleted, Archean lithosphere in all data sets: high shear wave velocities, high electrical resistivities, two-stage depleted mantle model ages that are dominantly > 2500 Ma, and lithospheric thickness estimates approaching and exceeding 200 km from petrological analysis of kimberlite-hosted mantle xenocrysts.

At the western and northern margins of the Gawler Craton, all data sets suggest a transition from cratonic core lithosphere to cratonic margin lithosphere, although the location of this transition differs slightly between data sets: in the V_{SV} model, the transition occurs approximately parallel to, but substantially inboard of, the conventionally-defined margin of the Gawler Craton; in the resistivity model, the transition approximately coincides with the trend of the Karari Shear Zone which separates Archean rocks to the south from Palaeoproterozoic rocks to the north; while the transition in the felsic and intermediate-to-mafic mantle model ages occurs approximately coincident with the conventionally-defined margin of the craton.

The southern Eyre Peninsula has distinctly different characteristics in the geophysical and isotopic models: lithospheric mantle V_{SV} velocities and resistivities are lower than they are in the cratonic core to the north, seemingly at odds with mantle model ages > 2500 Ma and an inferred petrological lithospheric thickness of ∼190–205 km in the central Eyre Peninsula. We suggest that stretching and metasomatism of the now southern Eyre Peninsula lithosphere during the Jurassic–Cretaceous separation of Australia and Antarctica might explain the conundrum: the mantle xenocrysts hosted in the Jurassic kimberlites and mantle model ages capture the pre-separation state of the lithosphere, in contrast to the geophysical techniques which 'see' the present-day Eyre Peninsula lithosphere.

The Curnamona Province displays relatively consistent patterns between the data sets largely suggestive of thick, depleted, Archean lithosphere. Intriguingly, the lithospheric mantle between the Gawler Craton and Curnamona Craton has characteristics indistinguishable from the cores of the Gawler Craton and Curnamona Province. This is surprising given the considerable thickness of Adelaide Superbasin sediments deposited in the rift basin between the Gawler Craton and Curnamona Province during Rodinia breakup. The data sets suggest that the lithosphere did not thin significantly between the Gawler Craton and Curnamona Craton, even though the rifting event was significant, and that there is a steep gradient in lithospheric thickness at latitude ∼33°S.

We observe that major IOCG deposits of the eastern Gawler Craton (e.g., Olympic Dam, Carrapateena, Hillside) reside above, or proximal to, a seismically slow uppermost lithospheric mantle layer underlain by the seismically fastest lithospheric mantle in the region. Major IOCG deposits of the Curnamona Province (e.g., North Portia, Kalkaroo) likewise reside above the seismically fastest lithospheric mantle in the region, albeit without the seismically slow uppermost lithospheric mantle layer. The inference of cool, thick, iron-depleted lithospheric mantle underlying major IOCG deposits of the Olympic Cu–Au Province, and Curnamona Province is consistent with partial melting of a precursor primed, metasomatised lithospheric mantle, with the melt products migrating upward to fertilise the uppermost mantle and/or lower crust according to accessible fluid pathways. The remnant seismic signatures of these processes might provide a useful precompetitive vector for IOCG prospectivity mapping.

Data and code availability

The Rayleigh wave phase velocity maps and shear velocity model described here are available on the South Australian Resources Information Gateway (https://map.sarig.sa.gov.au). The AusArray SA (https://doi.org/10.7914/sn/6k_2020) and Lake Eyre Basin array (https://doi.org/10.7914/sn/5g_2018) data are available on the Australian passive seismic server (AusPass; http://auspass.edu.au). SNAKEY (https://doi.org/10.7914/9j20-yq91) data will be available on AusPass from April 2028. Data from the ensuing list (experiment/network, network code, DOI - if any) of telemetered permanent seismic networks are available through AusPass and/or the Incorporated Research Institutions for Seismology Data Management Center (IRIS DMC; https://ds.iris.edu/ds/nodes/dmc): ANSN, AU; SAA, DU, 10.7914/SN/DU; AUSIS, S1, 10.7914/SN/ S1.

Competing interests

The authors have no competing interests.

References

Agrawal, S., Eakin, C. M., and O'Donnell, J. Characterizing the cover across South Australia: a simple passive-seismic method for estimating sedimentary thickness. *Geophysical Journal International*, 231(3):1850–1864, July 2022. doi: 10.1093/gji/ggac294.

Agrawal, S., Eakin, C. M., and O'Donnell, J. P. Tracking crustal thickness at the sediment inundated edge of the Gawler Craton, South Australia. *Tectonophysics*, 862:229938, Sept. 2023. doi: 10.1016/j.tecto.2023.229938.

Armistead, S. E., Betts, P. G., Ailleres, L., Armit, R. J., and Williams, H. A. Cu-Au mineralisation in the Curnamona Province, South Australia: A hybrid stratiform genetic model for Mesoproterozoic IOCG systems in Australia. *Ore Geology Reviews*, 94: 104–117, Mar. 2018. doi: 10.1016/j.oregeorev.2018.01.024.

Betts, P. G., Giles, D., Foden, J., Schaefer, B. F., Mark, G., Pankhurst, M. J., Forbes, C. J., Williams, H. A., Chalmers, N. C., and Hills, Q. Mesoproterozoic plume-modified orogenesis in eastern Precambrian Australia. *Tectonics*, 28(3), June 2009. doi: 10.1029/2008tc002325.

Budd, A. R. and Skirrow, R. G. The Nature and Origin of Gold Deposits of the Tarcoola Goldfield and Implications for the Central Gawler Gold Province, South Australia. *Economic Geology*, 102 (8):1541–1563, Dec. 2007. doi: 10.2113/gsecongeo.102.8.1541.

Capon, J. Analysis of Rayleigh-wave multipath propagation at LASA. *Bulletin of the Seismological Society of America*, 60(5): 1701–1731, Oct. 1970. doi: 10.1785/bssa0600051701.

Caroline M. Eakin and Robert Pickle. Seismic Network Around Kangaroo Eyre Yorke, 2023. doi: 10.7914/9J20-YQ91.

Chua, E. L. and Lebedev, S. Waveform tomography of the Antarctic Plate. *Geophysical Journal International*, 241(1):219–240, Jan. 2025. doi: 10.1093/gji/ggaf041.

Curtis, S. and Thiel, S. Identifying lithospheric boundaries using magnetotellurics and Nd isotope geochemistry: An example from the Gawler Craton, Australia. *Precambrian Research*, 320: 403–423, Jan. 2019. doi: 10.1016/j.precamres.2018.11.013.

de Laat, J. I., Lebedev, S., Celli, N. L., Bonadio, R., Chagas de Melo, B., and Rawlinson, N. Structure and evolution of the Australian plate and underlying upper mantle from waveform tomography with massive data sets. *Geophysical Journal International*, 234 (1):153–189, Feb. 2023. doi: 10.1093/gji/ggad062.

Dreiling, J. and Tilmann, F. BayHunter – McMC transdimensional Bayesian inversion of receiver functions and surface wave dispersion, V. 1.0. GFZ Data Services, 2019.

Dreiling, J., Tilmann, F., Yuan, X., Haberland, C., and Seneviratne, S. W. M. Crustal Structure of Sri Lanka Derived From Joint Inversion of Surface Wave Dispersion and Receiver Functions Using a Bayesian Approach. *Journal of Geophysical Research: Solid Earth*, 125(5), May 2020. doi: 10.1029/2019jb018688.

Eakin, C. Seismicity, Minerals, and Craton margins: The Lake Eyre Basin Seismic Deployment. *ASEG Extended Abstracts*, 2019(1): 1–2, Dec. 2019. doi: 10.1080/22020586.2019.12072989.

Eakin, C. M., Flashman, C., and Agrawal, S. Seismic anisotropy beneath Central Australia: A record of ancient lithospheric deformation. *Tectonophysics*, 820:229123, Dec. 2021. doi: 10.1016/j.tecto.2021.229123.

Eakin, C. M., Davies, D. R., Ghelichkhan, S., O'Donnell, J. P., and Agrawal, S. The Influence of Lithospheric Thickness Variations Beneath Australia on Seismic Anisotropy and Mantle Flow. *Geochemistry, Geophysics, Geosystems*, 24(9), Sept. 2023. doi: 10.1029/2023gc011066.

Eaton, D. W., Darbyshire, F., Evans, R. L., Grütter, H., Jones, A. G., and Yuan, X. The elusive lithosphere–asthenosphere boundary (LAB) beneath cratons. *Lithos*, 109(1–2):1–22, Apr. 2009. doi: 10.1016/j.lithos.2008.05.009.

Evernden, J. F. Direction of approach of Rayleigh waves and related problems: (Part I). *Bulletin of the Seismological Society of America*, 43(4):335–374, Oct. 1953. doi: 10.1785/bssa0430040335.

Fichtner, A., Kennett, B. L., Igel, H., and Bunge, H.-P. Full waveform tomography for radially anisotropic structure: New insights into present and past states of the Australasian upper mantle. *Earth and Planetary Science Letters*, 290(3–4):270–280, Feb. 2010. doi: 10.1016/j.epsl.2009.12.003.

Fichtner, A., Ritsema, J., and Thrastarson, S. A high-resolution discourse on seismic tomography. *Proceedings of the Royal Society A: Mathematical, Physical and Engineering Sciences*, 481(2320), Aug. 2025. doi: 10.1098/rspa.2024.0955.

Fishwick, S. and Rawlinson, N. 3-D structure of the Australian lithosphere from evolving seismic datasets. *Australian Journal of Earth Sciences*, 59(6):809–826, Aug. 2012. doi: 10.1080/08120099.2012.702319.

Forsyth, D. W. and Li, A. *Array analysis of two-dimensional variations in surface wave phase velocity and azimuthal anisotropy in the presence of multipathing interference*, page 81–97. American Geophysical Union, 2005. doi: 10.1029/157gm06.

Forsyth, D. W., Webb, S. C., Dorman, L. M., and Shen, Y. Phase Velocities of Rayleigh Waves in the MELT Experiment on the East Pacific Rise. *Science*, 280(5367):1235–1238, May 1998. doi: 10.1126/science.280.5367.1235.

Friederich, W., Wielandt, E., and Stange, S. Non-Plane Geometries of Seismic Surface Wavefields and Their Implications For Regional Surface-Wave Tomography. *Geophysical Journal International*, 119(3):931–948, Dec. 1994. doi: 10.1111/j.1365-246x.1994.tb04026.x.

Groves, D. I. and Santosh, M. *Mineral Systems, Earth Evolution, and Global Metallogeny*. Elsevier, 2023.

Groves, D. I., Bierlein, F. P., Meinert, L. D., and Hitzman, M. W. Iron Oxide Copper-Gold (IOCG) Deposits through Earth History: Implications for Origin, Lithospheric Setting, and Distinction from Other Epigenetic Iron Oxide Deposits. *Economic Geology*, 105 (3):641–654, May 2010. doi: 10.2113/gsecongeo.105.3.641.

Hand, M., Reid, A., and Jagodzinski, L. Tectonic Framework and Evolution of the Gawler Craton, Southern Australia. *Economic Geology*, 102(8):1377–1395, Dec. 2007. doi: 10.2113/gsecongeo.102.8.1377.

Hansen, S. E. and Emry, E. L. East Antarctic tectonic basin structure and its implications for ice-sheet modeling and sea-level projections. *Communications Earth & Environment*, 6(1), Feb. 2025. doi: 10.1038/s43247-025-02140-4.

Harmon, N., Forsyth, D. W., and Weeraratne, D. S. Thickening of young Pacific lithosphere from high-resolution Rayleigh wave tomography: A test of the conductive cooling model. *Earth and Planetary Science Letters*, 278(1–2):96–106, Feb. 2009. doi: 10.1016/j.epsl.2008.11.025.

Hartnady, M., Kirkland, C., Dutch, R., Bodorkos, S., and Jagodzinski, E. Evaluating zircon initial Hf isotopic composition using a combined SIMS–MC-LASS-ICP-MS approach: A case study from the Coompana Province in South Australia. *Chemical Geology*, 558:119870, Dec. 2020. doi: 10.1016/j.chemgeo.2020.119870.

Heinson, G., Didana, Y., Soeffky, P., Thiel, S., and Wise, T. The crustal geophysical signature of a world-class magmatic mineral system. *Scientific Reports*, 8(1), July 2018. doi: 10.1038/s41598-018-29016-2.

Heinson, G. S., Direen, N. G., and Gill, R. M. Magnetotelluric evidence for a deep-crustal mineralizing system beneath the Olympic Dam iron oxide copper-gold deposit, southern Australia. *Geology*, 34(7):573, 2006. doi: 10.1130/g22222.1.

Herrmann, R. B. Computer Programs in Seismology: An Evolving Tool for Instruction and Research. *Seismological Research Letters*, 84(6):1081–1088, Oct. 2013. doi: 10.1785/0220110096.

Hitzman, M. W., Oreskes, N., and Einaudi, M. T. Geological characteristics and tectonic setting of proterozoic iron oxide (Cu U Au REE) deposits. *Precambrian Research*, 58(1–4):241–287, Oct. 1992. doi: 10.1016/0301-9268(92)90121-4.

Huston, D. L., Blewett, R. S., and Champion, D. C. Australia through time: a summary of its tectonic and metallogenic evolution. *Episodes*, 35(1):23–43, Mar. 2012. doi: 10.18814/epiiugs/2012/v35i1/004.

Jagodzinski, E. A., Reid, A. J., Crowley, J. L., Wade, C. E., and Curtis, S. Precise zircon U-Pb dating of the Mesoproterozoic Gawler large igneous province, South Australia. *Results in Geochemistry*, 10:100020, Jan. 2023. doi: 10.1016/j.ringeo.2022.100020.

Kennett, B. L. N., Engdahl, E. R., and Buland, R. Constraints on seismic velocities in the Earth from traveltimes. *Geophysical Journal International*, 122(1):108–124, July 1995. doi: 10.1111/j.1365-246x.1995.tb03540.x.

Kennett, B. L. N., Fichtner, A., Fishwick, S., and Yoshizawa, K. Australian Seismological Reference Model (AuSREM): mantle component. *Geophysical Journal International*, 192(2):871–887, Dec. 2012. doi: 10.1093/gji/ggs065.

Kennett, B. L. N., Gorbatov, A., Yuan, H., Agrawal, S., Murdie, R., Doublier, M. P., Eakin, C. M., Miller, M. S., Zhao, L., Czarnota, K., O'Donnell, J. P., Dentith, M., and Gessner, K. Refining the Moho across the Australian continent. *Geophysical Journal International*, 233(3):1863–1877, Jan. 2023. doi: 10.1093/gji/ggad035.

Laske, G. Global observation of off-great-circle propagation of Long-Period surface waves. *Geophysical Journal International*, 123(1):245–259, Oct. 1995. doi: 10.1111/j.1365-246x.1995.tb06673.x.

Lay, T. and Kanamori, H. Geometric effects of global lateral heterogeneity on long-period surface wave propagation. *Journal of Geophysical Research: Solid Earth*, 90(B1):605–621, Jan. 1985. doi: 10.1029/jb090ib01p00605.

Lebedev, S., Adam, J. M.-C., and Meier, T. Mapping the Moho with seismic surface waves: A review, resolution analysis, and recommended inversion strategies. *Tectonophysics*, 609:377–394, Dec. 2013. doi: 10.1016/j.tecto.2012.12.030.

Li, A. and Burke, K. Upper mantle structure of southern Africa from Rayleigh wave tomography. *Journal of Geophysical Research: Solid Earth*, 111(B10), Oct. 2006. doi: 10.1029/2006jb004321.

Li, A., Forsyth, D. W., and Fischer, K. M. Shear velocity structure and azimuthal anisotropy beneath eastern North America from Rayleigh wave inversion. *Journal of Geophysical Research: Solid Earth*, 108(B8), Aug. 2003. doi: 10.1029/2002jb002259.

Liang, S. and Kennett, B. L. Passive seismic imaging of a craton edge – Central Australia. *Tectonophysics*, 797:228662, Dec. 2020. doi: 10.1016/j.tecto.2020.228662.

Lloyd, A. J., Wiens, D. A., Zhu, H., Tromp, J., Nyblade, A. A., Aster, R. C., Hansen, S. E., Dalziel, I. W. D., Wilson, T., Ivins, E. R., and O'Donnell, J. P. Seismic Structure of the Antarctic Upper Mantle Imaged with Adjoint Tomography. *Journal of Geophysical Research: Solid Earth*, 125(3), Mar. 2020a. doi: 10.1029/2019jb017823.

Lloyd, J. C., Blades, M. L., Counts, J. W., Collins, A. S., Amos, K. J., Wade, B. P., Hall, J. W., Hore, S., Ball, A. L., Shahin, S., and Drabsch, M. Neoproterozoic geochronology and provenance of the Adelaide Superbasin. *Precambrian Research*, 350:105849, Nov. 2020b. doi: 10.1016/j.precamres.2020.105849.

Magrini, F., Kästle, E., Pilia, S., Rawlinson, N., and De Siena, L. A New Shear-Velocity Model of Continental Australia Based on Multi-Scale Surface-Wave Tomography. *Journal of Geophysical Research: Solid Earth*, 128(7), June 2023. doi: 10.1029/2023jb026688.

Morrissey, L. J., Hand, M., Wade, B. P., and Szpunar, M. Early Mesoproterozoic metamorphism in the Barossa Complex, South Australia: links with the eastern margin of Proterozoic Australia. *Australian Journal of Earth Sciences*, 60(8):769–795, Dec. 2013. doi: 10.1080/08120099.2013.860623.

Myers, J. S., Shaw, R. D., and Tyler, I. M. Tectonic evolution of Proterozoic Australia. *Tectonics*, 15(6):1431–1446, Dec. 1996. doi: 10.1029/96tc02356.

O'Donnell, J., Stuart, G., Brisbourne, A., Selway, K., Yang, Y., Nield, G., Whitehouse, P., Nyblade, A., Wiens, D., Aster, R., Anandakrishnan, S., Huerta, A., Wilson, T., and Winberry, J. The uppermost mantle seismic velocity structure of West Antarctica from Rayleigh wave tomography: Insights into tectonic structure and geothermal heat flow. *Earth and Planetary Science Letters*, 522: 219–233, Sept. 2019. doi: 10.1016/j.epsl.2019.06.024.

O'Donnell, J., Thiel, S., Robertson, K., Gorbatov, A., and Eakin, C. Using seismic tomography to inform mineral exploration in South Australia: the AusArray SA broadband seismic array. *MESA J.*, 93(2):24–31, 2020.

O'Donnell, J., Agrawal, S., Eakin, C., Thiel, S., Brand, K., Gorbatov, A., and Goleby, B. Mapping crustal structure across southern Australia using seismic ambient noise tomography. *Gondwana Research*, 121:307–324, Sept. 2023. doi: 10.1016/j.gr.2023.04.013.

Pollett, A., Thiel, S., Bendall, B., Raimondo, T., and Hand, M. Mapping the Gawler Craton–Musgrave Province interface using integrated heat flow and magnetotellurics. *Tectonophysics*, 756: 43–56, Apr. 2019. doi: 10.1016/j.tecto.2019.02.017.

Preiss, W. The Adelaide Geosyncline of South Australia and its significance in Neoproterozoic continental reconstruction. *Precambrian Research*, 100(1–3):21–63, Mar. 2000. doi: 10.1016/s0301-9268(99)00068-6.

Preiss, W., Korsch, R., Blewett, R., Fomin, T., Cowley, W., Neumann, N., and Meixner, A. Geological interpretation of deep seismic reflection line 09GA-CG1: the Curnamona Province-Gawler Cra-

ton Link Line, South Australia. *Geoscience Australia Record*, 10: 66–76, 2010.

Preiss, W. V., Belperio, A. P., Cowley, W. M., and Rankin, L. R. Neoproterozoic. In Drexel, J. F., Preiss, W. V., and Parker, A. J., editors, *The Geology of South Australia: The Precambrian*, volume 1, chapter 6, pages 171–203. Geological Survey of South Australia, 1993.

Rawlinson, N., Salmon, M., and Kennett, B. Transportable seismic array tomography in southeast Australia: Illuminating the transition from Proterozoic to Phanerozoic lithosphere. *Lithos*, 189: 65–76, Feb. 2014. doi: 10.1016/j.lithos.2013.06.001.

Rawlinson, N., Pilia, S., Young, M., Salmon, M., and Yang, Y. Crust and upper mantle structure beneath southeast Australia from ambient noise and teleseismic tomography. *Tectonophysics*, 689:143–156, Oct. 2016. doi: 10.1016/j.tecto.2015.11.034.

Reid, A. The Olympic Cu-Au Province, Gawler Craton: A Review of the Lithospheric Architecture, Geodynamic Setting, Alteration Systems, Cover Successions and Prospectivity. *Minerals*, 9(6): 371, June 2019. doi: 10.3390/min9060371.

Reid, A. J. and Hand, M. Mesoarchean to Mesoproterozoic evolution of the southern Gawler Craton, South Australia. *Episodes*, 35(1):216–225, Mar. 2012. doi: 10.18814/epiiugs/2012/v35i1/021.

Selway, K. On the Causes of Electrical Conductivity Anomalies in Tectonically Stable Lithosphere. *Surveys in Geophysics*, 35(1): 219–257, May 2013. doi: 10.1007/s10712-013-9235-1.

Selway, K., Özaydın, S., and Payne, J. Metasomatism and depletion of the southern Gawler Craton from combined mantle xenocryst and AusLAMP magnetotelluric data. *Exploration Geophysics*, 55 (5):602–616, Sept. 2024. doi: 10.1080/08123985.2023.2282711.

Simons, F. J. and van der Hilst, R. D. Age-dependent seismic thickness and mechanical strength of the Australian lithosphere. *Geophysical Research Letters*, 29(11), June 2002. doi: 10.1029/2002gl014962.

Sippl, C. Moho geometry along a north–south passive seismic transect through Central Australia. *Tectonophysics*, 676:56–69, Apr. 2016. doi: 10.1016/j.tecto.2016.03.031.

Skirrow, R. G. Iron oxide copper-gold (IOCG) deposits – A review (part 1): Settings, mineralogy, ore geochemistry and classification. *Ore Geology Reviews*, 140:104569, Jan. 2022. doi: 10.1016/j.oregeorev.2021.104569.

Skirrow, R. G., Bastrakov, E. N., Barovich, K., Fraser, G. L., Creaser, R. A., Fanning, C. M., Raymond, O. L., and Davidson, G. J. Timing of Iron Oxide Cu-Au-(U) Hydrothermal Activity and Nd Isotope Constraints on Metal Sources in the Gawler Craton, South Australia. *Economic Geology*, 102(8):1441–1470, Dec. 2007. doi: 10.2113/gsecongeo.102.8.1441.

Skirrow, R. G., van der Wielen, S. E., Champion, D. C., Czarnota, K., and Thiel, S. Lithospheric Architecture and Mantle Metasomatism Linked to Iron Oxide Cu-Au Ore Formation: Multidisciplinary Evidence from the Olympic Dam Region, South Australia. *Geochemistry, Geophysics, Geosystems*, 19(8):2673–2705, Aug. 2018. doi: 10.1029/2018gc007561.

Spetzler, J., Trampert, J., and Snieder, R. Are we exceeding the limits of the Great Circle Approximation in global surface wave tomography? *Geophysical Research Letters*, 28(12):2341–2344, June 2001. doi: 10.1029/2000gl012691.

Sudholz, Z. J., Yaxley, G. M., Jaques, A. L., Cooper, S. A., Czarnota, K., Taylor, W. R., Chen, J., and Knowles, B. M. Multi-Stage Evolution of the South Australian Craton: Petrological Constraints on the Architecture, Lithology, and Geochemistry of the Lithospheric Mantle. *Geochemistry, Geophysics, Geosystems*, 23(11), Nov. 2022. doi: 10.1029/2022gc010558.

Sun, W. and Kennett, B. L. N. Uppermost mantle structure of the Australian continent from Pn traveltime tomography. *Journal of Geophysical Research: Solid Earth*, 121(3):2004–2019, Mar. 2016. doi: 10.1002/2015jb012597.

Szpunar, M., Wade, B., Hand, M., and Barovich, K. Timing of Proterozoic high-grade metamorphism in the Barossa Complex, southern South Australia: exploring the extent of the 1590 Ma event. *MESA J.*, 47:21–27, 2007.

Thiel, S., Reid, A., Heinson, G., and Robertson, K. Insights into lithospheric architecture, fertilisation and fluid pathways from AusLAMP MT. *ASEG Extended Abstracts*, 2016(1):1–6, Dec. 2016. doi: 10.1071/aseg2016ab261.

van der Hilst, R., Kennett, B., Christie, D., and Grant, J. Project Skippy explores lithosphere and mantle beneath Australia. *Eos, Transactions American Geophysical Union*, 75(15):177–181, Apr. 1994. doi: 10.1029/94eo00857.

Wade, B., Kelsey, D., Hand, M., and Barovich, K. The Musgrave Province: Stitching north, west and south Australia. *Precambrian Research*, 166(1–4):370–386, Oct. 2008. doi: 10.1016/j.precamres.2007.05.007.

Wade, C., Corrick, A., Gouthas, G., Wise, T., and Dutch, R. Sm-Nd isotopic data for South Australia: dataset and report. *MESA J.*, 98:29–038, 2024.

Wade, C. E. Definition of the mesoproterozoic ninnerie supersuite, Curnamona Province, South Australia. *Mesa J.*, 62:25–42, 2011.

Wade, C. E., Reid, A. J., Wingate, M. T., Jagodzinski, E. A., and Barovich, K. Geochemistry and geochronology of the c. 1585Ma Benagerie Volcanic Suite, southern Australia: Relationship to the Gawler Range Volcanics and implications for the petrogenesis of a Mesoproterozoic silicic large igneous province. *Precambrian Research*, 206–207:17–35, June 2012. doi: 10.1016/j.precamres.2012.02.020.

Wade, C. E., Payne, J. L., Barovich, K. M., and Reid, A. J. Heterogeneity of the sub-continental lithospheric mantle and 'non-juvenile' mantle additions to a Proterozoic silicic large igneous province. *Lithos*, 340–341:87–107, Sept. 2019. doi: 10.1016/j.lithos.2019.05.005.

Wade, C. E., Payne, J. L., Barovich, K., Gilbert, S., Wade, B. P., Crowley, J. L., Reid, A., and Jagodzinski, E. A. Zircon trace element geochemistry as an indicator of magma fertility in iron oxide copper-gold provinces. *Economic Geology*, 117(3):703–718, May 2022a. doi: 10.5382/econgeo.4886.

Wade, C. E., Payne, J. L., Barovich, K. M., Reid, A. J., Jagodzinski, E. A., Curtis, S., and Hill, J. Temporal, geochemical and isotopic constraints on plume-driven felsic and mafic components in a Mesoproterozoic flood rhyolite province. *Results in Geochemistry*, 9:100019, Oct. 2022b. doi: 10.1016/j.ringeo.2022.100019.

Weeraratne, D. S., Forsyth, D. W., Fischer, K. M., and Nyblade, A. A. Evidence for an upper mantle plume beneath the Tanzanian craton from Rayleigh wave tomography. *Journal of Geophysical Research: Solid Earth*, 108(B9), Sept. 2003. doi: 10.1029/2002jb002273.

Wei, Z., Kennett, B. L. N., and Sun, W. Sn-wave velocity structure of the uppermost mantle beneath the Australian continent. *Geophysical Journal International*, 213(3):2071–2084, Mar. 2018. doi: 10.1093/gji/ggy109.

Williams, H., Stewart, J., and Betts, P. Imposition of a Proterozoic salient on a Palaeozoic orogen at the eastern margin of Gondwana. *Gondwana Research*, 16(3–4):669–686, Dec. 2009. doi: 10.1016/j.gr.2009.06.006.

Wise, T. and Thiel, S. Proterozoic tectonothermal processes imaged with magnetotellurics and seismic reflection in southern Australia. *Geoscience Frontiers*, 11(3):885–893, May 2020. doi: 10.1016/j.gsf.2019.09.006.

Woodhouse, J. H. and Wong, Y. K. Amplitude, phase and path anomalies of mantle waves. *Geophysical Journal International*, 87(3):753–773, Dec. 1986. doi: 10.1111/j.1365-246x.1986.tb01970.x.

Yang, Y. and Forsyth, D. W. Regional tomographic inversion of the amplitude and phase of Rayleigh waves with 2-D sensitivity kernels. *Geophysical Journal International*, 166(3):1148–1160, Sept. 2006a. doi: 10.1111/j.1365-246x.2006.02972.x.

Yang, Y. and Forsyth, D. W. Rayleigh wave phase velocities, small-scale convection, and azimuthal anisotropy beneath southern California. *Journal of Geophysical Research: Solid Earth*, 111 (B7), July 2006b. doi: 10.1029/2005jb004180.

Yoshizawa, K. Radially anisotropic 3-D shear wave structure of the Australian lithosphere and asthenosphere from multi-mode surface waves. *Physics of the Earth and Planetary Interiors*, 235: 33–48, Oct. 2014. doi: 10.1016/j.pepi.2014.07.008.

Yoshizawa, K. and Kennett, B. L. N. The lithosphere-asthenosphere transition and radial anisotropy beneath the Australian continent. *Geophysical Research Letters*, 42(10):3839–3846, May 2015. doi: 10.1002/2015gl063845.

Zielhuis, A. and Hilst, R. D. Upper-mantle shear velocity beneath eastern Australia from inversion of waveforms from SKIPPY portable arrays. *Geophysical Journal International*, 127(1):1–16, Oct. 1996. doi: 10.1111/j.1365-246x.1996.tb01530.x.